Stress Granule Sequestration of CCR4–NOT Promotes Poly(A) Lengthening of Stress-Survival Transcripts

Yi-Cheng Tsai[1,2,3], Hiroyuki Uechi[4,7,†], Sean R. Millar[1,2], Eileigh Kadijk[1], Alon Minkovich[1,2], John Paul Tsu Ouyang[5], Karl J. Schreiber[1], Jie Qi Huang[1,2], Carina A. Lyons[1,2], Vesal Kasmaeifar[2], Zhixin Zhang[6], Rico Barsacchi[7], Claudia Möbius[7], Antje Janosch[7], Jonathan C. Savage[7], Olivia S. Rissland[5], Hannes Röst[2,3], Anthony A. Hyman[7,8*], Ji-Young Youn[1,2,8,9*]

[1] Program in Molecular Medicine, The Hospital for Sick Children, Toronto, ON M5G 0A4, Canada.

[2] Department of Molecular Genetics, University of Toronto, Toronto, ON M5S 1A8, Canada.

[3] Terrence Donnelly Centre for Cellular Biomolecular Research, University of Toronto, Toronto, ON M5S 3E1, Canada.

[4] Frontier Research Institute for Interdisciplinary Sciences, Tohoku University, Sendai, Japan

[5] Department of Biochemistry & Molecular Genetics, University of Colorado School of Medicine, Aurora, CO 80045, USA; RNA Bioscience Initiative, University of Colorado School of Medicine, Aurora, CO 80045, USA.

[6] 4+4 Medical Doctor Program, Chinese Academy of Medical Sciences and Peking Union Medical College, Beijing, China.

[7] Max Planck Institute of Molecular Cell Biology and Genetics, 01307, Dresden, Germany

[8] Senior Author

[9] Lead Contact: jiyoung.youn@sickkids.ca

[†]Present Address: Graduate School of Pharmaceutical Sciences, Kyoto University, 606-8501 Kyoto, Japan

* Corresponding authors

KEYWORDS: stress granules, CCR4-NOT complex, poly(A) tail regulation, condensate proteome, protein localization, proximity-dependent biotinylation, lipoamide, data-independent acquisition.

Data deposition: Mass spectrometry data have been deposited in the Mass Spectrometry Interactive Virtual Environment (MassIVE, http://massive.ucsd.edu).

MassIVE ID: MSV000095953 (ftp://massive.ucsd.edu/v08/MSV000095953/)

MassIVE ID: MSV000095944 (ftp://massive.ucsd.edu/v08/MSV000095944/)

MassIVE ID: MSV000098662 (ftp://massive-ftp.ucsd.edu/v10/MSV000098662/)

MassIVE ID: MSV000100193 (ftp://massive-ftp.ucsd.edu/v11/MSV000100193/)

ABSTRACT

Cells adapt to stress by rewiring their post-transcriptional gene regulation. Stress granules—biomolecular condensates composed of polyadenylated RNAs and RNA-binding proteins—are implicated in this process, yet their precise functional roles remain debated. To address this, we mapped the dynamic proteomic landscapes of stress granules formed under oxidative and hyperosmotic stress using multi-bait BioID proximity profiling coupled with quantitative mass spectrometry. This analysis revealed context-specific remodeling of proximal interaction networks and identified a conserved, stress-dependent shift in association with the CCR4–NOT deadenylase complex. A complementary genome-wide chemical genetic screen further implicated CCR4-NOT in stress granule biology, showing that reduced CCR4–NOT activity bypassed lipoamide-mediated inhibition of stress granule assembly. Microscopy showed sequestration of the CCR4-NOT complex into stress granules, and global transcriptomic analyses revealed that this relocalization promotes poly(A) tail lengthening and increased abundance of stress-induced survival transcripts. Together, integration of proteomics, chemical genetics, and transcriptomics uncovers a spatial mechanism by which stress granule assembly promotes cellular adaptation to stress through sequestration of CCR4-NOT from the cytosol and consequent remodeling of post-transcriptional regulation.

49 **MAIN**

50 Living organisms have evolved mechanisms to survive unfavourable conditions. At the cellular level,
51 adaptation to stress involves rewiring transcriptional programming, translation control, signaling,
52 metabolism, and the reorganization of subcellular proteomes. Cells shift biological processes to conserve
53 resources during stress, slowing global transcription and translation to minimize energy consumption while
54 actively transcribing genes involved in stress responses[1,2].

55 Cellular adaptation involves changes in the subcellular proteome organization[3-5]. Advances in spatial
56 proteomics, including imaging-based microscopy and mass spectrometry, have enabled the identification
57 of proteins localized to specific subcellular compartments[4,6-12]. During stress, proteins dynamically
58 exchange between compartments[5,13-16]; however, assigning functional roles to these localization changes
59 remains challenging.

60 The re-organization of subcellular proteomes often involves the formation of membraneless organelles
61 or biomolecular condensates, which concentrate biomolecules through liquid-liquid phase separation[17-20].
62 By enriching specific biomolecules, biomolecular condensates can increase or decrease biochemical
63 reactions, buffer protein concentrations, sense environmental changes, and provide mechanical forces[21-
64 25]. Stress granules are cytosolic biomolecular condensates or RNA granules that transiently form in
65 response to various stress conditions, often as a product of global translation shutdown and release of
66 mRNAs from the polysome pool[26,27]. Stress granules host hundreds of proteins and several thousand
67 transcripts[28-31] and are central to stress response, linking translation control to signaling and immune
68 responses[29,32,33]. They host antiviral responses during viral infection[27] and sequester regulators of cell
69 death[34,35] or cell growth pathway components during stress[36].

70 Elucidating stress granule function is confounded by the variability observed depending on the cellular
71 stress or cell type[29,37]. For example, depending on how translation is blocked, stress granules vary in their
72 composition of translation initiation factors. Activation of the integrated stress response and eIF2α
73 phosphorylation induces stress granules lacking eIF2-eIF5-Met-tRNA^{Met} ternary complex, while eIF4A
74 poisons (e.g., Pateamine A) induce stress granules containing this ternary complex. Stress granules
75 induced by chemotherapeutic drugs, such as selenite, UV and other xenobiotic agents, lack eIF3[29,38]. Lastly,
76 hyperosmotic stress induces phospho-eIF2α-independent stress granules through molecular crowding;

77 however, stress granules induced by hyperosmotic stress is poorly characterized. This underscores the
78 importance of studying stress granules induced by distinct mechanisms.

79 A key aspect of the stress response is the upregulation of proteins required for adaptation, including
80 chaperones and transcription factors that promote cell survival[26,39-43]. However, how the corresponding
81 mRNAs evade mRNA decay pathways to maintain high abundance and preferential translation remains
82 unclear.

83 As part of post-transcriptional regulation, modulation of poly(A) tail lengths is crucial for protecting mRNA
84 from decay[44]. Poly(A) tail lengths are controlled by a balance between the action of cytoplasmic poly(A)
85 RNA polymerase (*e.g.,* GLD2 and TENT5B) that elongate these tails and deadenylases (*i.e.,* CCR4-NOT,
86 PAN2-3 complexes and PARN) that shorten them[44,45]. Among these three deadenylases in vertebrates [44],
87 the CCR4-NOT complex is the principal deadenylation responsible for degrading poly(A)s[44-46]. According
88 to a biphasic model of deadenylation, the PAN2-PAN3 complex initiates the poly(A) tail removal, while the
89 CCR4-NOT complex trims the remaining tail close to the 3'-UTR[47]. The CCR4-NOT complex consists of
90 eleven subunits, with a conserved core formed by two major modules: the NOT module (comprising the
91 scaffolding protein CNOT1 and a CNOT2-CNOT3 heterodimer) and the catalytic module (one of the
92 deadenylase CCR4 units, CNOT6 or CNOT6L, paired with one of the exonuclease CAF1 units, CNOT7 or
93 CNOT8). The CNOT6, CNOT6L, CNOT7 and CNOT8 subunits perform the deadenylase activity[44], while
94 the NOT module (CNOT1, CNOT2, CNOT3) is critical for maintaining complex integrity, regulating the
95 catalytic module's activity, and recruiting the complex to specific mRNAs via specific interactions with RNA-
96 binding or GW182 proteins[48-55].

97 Acute stress induces poly(A) tail lengthening[56-59]. While stress-induced stabilization of transcripts has
98 been linked to inhibiting deadenylation[58,60], the molecular mechanisms behind stress-induced poly(A) tail
99 lengthening remain elusive. Recent work has demonstrated that poly(A) tail extension is a prerequisite for
100 stress granule assembly[61], hinting at a potential link between stress response and the regulation of
101 enzymes controlling poly(A) lengths. However, clear evidence connecting poly(A) tail regulatory pathways
102 to stress responses remains limited.

103 Recently, multi-bait proteomics has become a powerful approach for studying protein localization within
104 condensates[62,63]. In this study, we use multi-bait BioID time course experiments to map the proximal

105 interactome of stress granule proteins, providing a resource that captures proteomic landscape changes
106 during stress. Leveraging this resource, we demonstrate that interactions with the CCR4-NOT complex shift
107 dynamically in response to stress. A complementary genome-wide CRISPR screen against stress granule-
108 inhibiting chemical lipoamide revealed that the removal of CCR4-NOT stabilizes stress granules through
109 poly(A) tail lengthening. Microscopy analysis of CCR4-NOT showed poor localization to P-bodies, contrary
110 to its annotation, but strong localization to stress granules during stress. We propose that stress granules
111 promote cellular adaptation by sequestering the CCR4–NOT complex, attenuating its deadenylase activity
112 and enabling poly(A) tail lengthening that sustains transcripts important for cell survival.
113

114 **RESULTS**

115 **Dynamic Changes in Proximal Interactions of Stress Granule Proteins.**

116 We examined the proximal interaction networks of stress granule proteins G3BP1 and FMR1 during
117 oxidative stress. Previously, we reported that the proximal interactions of G3BP1 and EIF4A1 remained
118 largely unchanged before and after stress granule assembly when using the slow biotin ligase BirA* [63].
119 However, this approach involved a labeling period significantly longer than the known kinetics of stress
120 granule assembly. To capture these interactions more accurately, we employed the faster biotin ligase,
121 miniTurbo[64], which enables proximal labeling within 15-30 min, compared to the 3–24 h required by BirA*.
122 We integrated expression constructs of G3BP1 and FMR1, each fused to miniTurbo-3xFLAG (miniT), into
123 the inducible Flp-In locus T-REx HEK293 system. The expression levels of miniT-tagged proteins were
124 comparable to their endogenous counterparts (Figure S1A), increasing total protein abundance by about
125 two-fold. Since G3BP1 is known to scaffold stress granule assembly, we checked if miniT-G3BP1 induction
126 induces stress granule assembly in the absence of stress and found no visible stress granules (Figure
127 S1B).

128 To assess proximal interaction changes upon stress granule assembly, we induced bait protein
129 expression in biotin-depleted media and pulse-labeled for 30 min in either no stress condition (T1) or 5 min
130 into oxidative stress induced with 0.5mM sodium arsenite (III) (T2; Figure 1A; see Methods). Proteins
131 biotinylated during T1 displayed a general cytoplasmic distribution, whereas during T2, they were highly
132 enriched in cytosolic puncta, colocalizing with the stress granule marker TIAR (Figure S1B).

133 Biological duplicates of G3BP1, FMR1, and negative controls (miniT alone, miniT-GFP, and parental
134 cells) were processed for BioID coupled to mass spectrometry (MS) followed by SAINTexpress analysis[65,66]
135 to determine high-confidence proximal interactors (BFDR ≤0.05). G3BP1 and FMR1 identified 137 and 102
136 high-confidence interactors during no stress and 107 and 139 during stress, respectively (Table S1, BFDR
137 ≤0.05).
138 Most proximal interactors remained similar in abundance as reported[37,63], confirming pre-existing
139 proximal interactions between stress granule components in the absence of microscopically visible
140 condensates. However, the improved labeling kinetics of the miniTurbo enzyme revealed a higher fraction
141 of interactors displaying stress-dependent abundance changes. Approximately 4% and 30% of G3BP1
142 interactors, as well as 34% and 15% of FMR1 interactors, displayed ≥1.5-fold increase or decrease in
143 abundance, respectively (Figure 1B). Common changes in G3BP1 and FMR1's stress BioID profiles
144 included shared increased interactors (*e.g.,* BICC1, TRIM56) and decreased interactors (*e.g.,* CNOT1,
145 CNOT2, CNOT3, CNOT4). These findings indicate coordinated dynamic rearrangements in proximal
146 interaction networks as G3BP1 and FMR1 condense to form stress granules.
147
148 **Stress-Induced Proximal Interaction Changes Are Reversed by Stress Granule Inhibitor, Lipoamide.**
149 Most stress-induced changes common to G3BP1 and FMR1 are abundance changes (~1.5-3-fold
150 changes in spectral counts) rather than their complete situational absence or presence (Figure 1B). To
151 examine if these observed abundance changes reflect dynamic molecular interactions associated with
152 stress granule assembly, we repeated the BioID experiment under the stress granule-inhibiting effects of
153 lipoamide. Lipoamide is an antioxidant that prevents stress granule assembly during oxidative stress by
154 blocking the oxidation of proteins. This mechanism primarily acts on intrinsically disordered proteins, such
155 as SRSF1 and SFPQ. The redox state of the latter influences stress granule formation[67].
156 Titration tests of potassium arsenate (As(V)), and lipoamide were used to identify effective
157 concentrations for inhibiting stress granule assembly in HEK293 BioID miniT-GFP and miniT-G3BP1 cells.
158 Note that all experiments involving lipoamide were used alongside the pentavalent form of As(V) (*e.g.,*
159 potassium arsenate or sodium arsenate), which is a weaker oxidizer than the trivalent form of As(III) (*e.g.,*
160 sodium arsenite). It was necessary to increase lipoamide concentration to fully inhibit stress granule

161 assembly as potassium arsenate levels rose (Figure S1C). Based on these tests, cells were pre-treated
162 with 100 μM lipoamide before inducing stress with 1 mM potassium arsenate (As(V)), followed by 30 min
163 biotin labeling. Pre-treatment with a DMSO control followed by As(V) stress induced abundance changes
164 in G3BP1 proximal interactions (*e.g.,* TRIM56, BICC1, CCR4-NOT complex components) that paralleled
165 those seen during As(III) stress (Figure 1C, top). However, when pre-treated with lipoamide, interaction
166 profiles remained at no stress levels and failed to recapitulate any stress-induced changes (Figure 1C,
167 bottom). Further, lipoamide pre-treatment had no effect on G3BP1's interaction profile during no stress
168 (Figure S1D). We propose that lipoamide's modulation of the redox state of stress granule proteins inhibits
169 stress-induced changes in the G3BP1 proximal interaction network. These findings indicate that the
170 observed abundance changes in G3BP1 and FMR1's BioID profiles reflect dynamic molecular
171 rearrangements during stress granule assembly.
172
173 **Mapping the Dynamic Stress Granule Interactome During Oxidative and Hyperosmotic Stress**
174 The oxidative stress-induced changes in G3BP1's interaction profile were similarly observed during
175 FMR1 BioID. We adopted a multi-bait experimental design to extensively define the dynamic stress granule
176 proximal interaction network. Nine baits known to localize to stress granules, or their related condensates,
177 were selected with the criteria of maximizing the identification of stress granule proteins. Combining these
178 baits (CELF1, DAZL, CNOT2, YTHDF2, ZC3HAV1, G3BP1, DDX3X, EIF4A2 and FMR1; Figure 1D; see
179 Methods) was predicted to recover 60% of high-confidence interactors identified in no stress BioID dataset
180 using 58 BirA*-conjugated baits[63] (with the assumption that miniTurbioID provides similar labeling profiles),
181 and 87% of the literature-curated stress granule proteome (Figure S1E, Table S2).
182 To investigate the effect of stress context in stress granules' interaction networks, we incorporated two
183 stressors - oxidative and hyperosmotic – with distinct stress granule induction mechanisms into our BioID
184 screens. This approach aimed to identify both conserved and unique proteomic changes associated with
185 distinct stress granule assembly pathways. Oxidative stress induces stress granules by the scaffolding of
186 key nucleator proteins (G3BP1/2) and activation of the integrated stress response. Interfering with either of
187 these, by means of knockout (G3BP1Δ, G3BP2Δ) or loss-of-function mutation (eIF2α S51A)[68,69], is
188 sufficient to curtail stress granule assembly. In contrast, hyperosmotic stress does not depend on G3BP1/2

189 nucleators or eIF2α phosphorylation[68-70] (Figure 1E). Instead, the resulting cellular crowding during
190 hyperosmotic stress drives stress granule nucleation[71,72]. In general, the cellular changes caused by
191 oxidative *vs.* hyperosmotic stresses are distinct; oxidative stress creates reactive oxygen species, which
192 damages cellular biomolecules and organelles[73-75], while hyperosmotic stress induces immediate loss of
193 water and activation of condensates inducing regulatory volume increase to compensate for volume
194 loss[76,77].

195 Accordingly, we performed separate BioID time course experiments to measure the dynamic
196 rearrangement of the stress granule proximal interaction network during exposure and recovery from both
197 stressors. We performed biotin labeling 5 min into oxidative stress for 30 min (T2_As(III)) and 1h after
198 recovering from oxidative stress (T3_As(III)) based on our estimate of dissolution kinetics (Figure S2A) and
199 published report[78]. For hyperosmotic stress, we noted small stress granules forming upon exposure to 0.2M
200 NaCl, with growth observed up to 45 min into stress (Figure S2B). We observe robust
201 eIF2α phosphorylation upon 30 min of exposure to oxidative stress and a moderate increase after 60 min
202 of hyperosmotic stress (Figure 1F). Biotin labeling commenced 45 min into NaCl stress for 30 min
203 (T2_NaCl), and we confirmed the enrichment of biotinylated proteins in NaCl-induced stress granules
204 (Figure S2C). Upon removal of hyperosmotic stress, stress granules rapidly disassembled (Figure S2D).
205 Consequently, we initiated biotin labeling immediately after hyperosmotic stress removal (T3_NaCl; Figure
206 S2E). The differences in disassembly kinetics between oxidative (As(III)) and hyperosmotic (NaCl) stress
207 correlated with faster translational resumption following hyperosmotic stress recovery (Figure S2F).

208 Nine baits localizing to stress granules or stress granules and P-bodies were stably and inducibly
209 expressed in HEK293 cells in biotin-depleted media. The cells underwent 30 min of biotin pulse labelling at
210 various time points (T1-3) under oxidative (As(III)) or hyperosmotic (NaCl) stress, along with negative
211 controls (miniTurbo alone and miniTurbo-GFP) (Figure 1E, Figure S2E, S2G). We identified 5,605 high-
212 confidence proximal interactions across 45 bait-stress conditions and 754 preys (BFDR ≤ 0.05
213 SAINTexpress, Table S3) using mass spectrometry data acquired in conventional Data-Dependent
214 Acquisition (DDA) mode, followed by SAINT analysis. Gene Ontology (GO) analysis revealed terms related
215 to stress granules (cytoplasmic stress granule; GO:0010494, mRNA binding; GO:0003729, translation;
216 GO:0006412), and unanticipated terms like microtubule organizing center (GO:0005815) and microtubule

217 cytoskeleton (GO: 0015630) (Table S3). The significance of microtubules and motor proteins in stress
218 granule assembly has been previously documented for stress granules induced by oxidative stress[79,80].
219 However, in this dataset, proximal interactions with microtubule proteins were encountered specifically
220 during the T2_NaCl timepoint (example of DDX3X BioID in Figure S3A).

221 To see if these interactions with microtubule-associated proteins are unique to "mature" stress granules
222 formed later in stress, we performed BioID in DDX3X-miniT at an earlier time point (5-35 min post-NaCl
223 exposure) and found similar results. These interactions were reproduced during hyperosmotic stress
224 induced by sorbitol (0.4M) (Figure S3B, Table S3), indicating that DDX3X's increased association with
225 microtubule and centrosome proteins is a general response to hyperosmotic stress. To assess whether
226 these interactions were a non-specific result of hyperosmotic stress-mediated molecular crowding, we
227 examined the proximal interactions of the P-body marker DCP1A. We did not find significant enrichment of
228 microtubule-associated proteins in DCP1A hyperosmotic stress BioID data, suggesting this change is
229 unique to stress granule baits (Figure S3C, Table S3).

230

231 **Quantitative Analysis of Stress BioID**

232 ***A. Identification of High-Confidence Interactions using SAINTq***

233 Under the initial DDA-based analytical framework, a large portion of the dataset was marked by missing
234 values across different stress time points, likely due to the semi-stochastic nature of DDA mass
235 spectrometry (Figure S4A). To improve the quantitative analysis, we re-analyzed our BioID samples using
236 Data-Independent Acquisition (DIA) mode in the mass spectrometer. We built a quantitative DIA analysis
237 workflow tailored to BioID samples to accommodate the frequent variability in interactor abundance and
238 identity among different baits. In brief, DIA output was deconvoluted with DIA-NN[81] for protein identification
239 and quantification, analyzed with SAINTq[82] to define high-confidence interactors, and linear-mixed model
240 ANOVA to identify significant quantitative changes (Figure 2A**;** Figure S4B**;** see Methods).

241 With DIA, we improved detection sensitivity and data completeness (Figure S4C-D). Biological replicates
242 showed high reproducibility, with correlation coefficients ranging from 0.853 to 0.963 (Figure S5). After
243 SAINTq analysis, we identified over 2,000 novel interactors compared to previously reported stress granule
244 datasets generated using proximity-dependent biotinylation techniques (Figure 2B). Separating high-

245 confidence interactors based on the stress condition revealed that the majority of the novel interactors are
246 identified in the hyperosmotic stress condition (T2_NaCl). Comparisons of high-confidence interactors
247 (BFDR ≤ 0.03, SAINTq) identified in no stress (T1) against those in oxidative (T2_As(III)) or hyperosmotic
248 stress (T2_NaCl) show a two-fold increase in interactors unique to T2_NaCl (≥1 bait; Figure 2C). These
249 results indicate that the dynamic rearrangements in the stress granule proximal interaction networks
250 depend on the stress context.

251 To accurately discern stress granule-relevant interactions, we filtered for high-confidence interactors
252 identified by multiple stress granule baits (BFDR ≤ 0.03; ≥ 2 baits). Under these criteria, DIA-SAINTq
253 analysis identified 13,836 high-confidence bait-prey interactions across the entire BioID dataset, comprising
254 1,801 unique preys (Table S4). This yields a bait-specific recovery rate of 10-64% of the protein-protein
255 interactions annotated in BioGRID, with stress time points observing marginally greater recovery (Table
256 S4).

257 The BioID data is well visualized by hierarchical clustering analysis of the bait-condition and prey
258 abundance matrix (Figure 2D; see Methods). Bait-condition combinations primarily clustered according to
259 bait protein, rather than stress condition, indicating that each bait maintains a distinct labeling profile
260 regardless of state changes. However, all baits (except CNOT2) resolve into two distinct clusters during
261 hyperosmotic stress (top gray boxes 1 and 2 in Figure 2D). This clustering of T2_NaCl samples is attributed
262 to proximal interactors exhibiting greater abundances (red boxes) compared to their T1, T2_As(III), or T3
263 sample analogs (green boxes; Figure 2D).

264 High-confidence preys cluster into four large groups characterized by distinct GO term enrichment
265 (Figure 2E, Table S5). Cluster 3 preys are most abundant and comprise known stress granule components.
266 Expectedly, these are enriched for terms including “cytoplasmic ribonucleoprotein granule” (GO:0036464)
267 and “stress granule assembly” (GO:0034063). Cluster 1 is similarly defined by GO terms relevant to stress
268 granule biology, such as “mRNA 3’ UTR binding” (GO:0003730), but also unexpected terms like
269 “cytoplasmic large ribosomal subunit” (GO:0022625). An enrichment for proteins associated with the
270 “microtubule cytoskeleton” (GO:0015630) and those presenting “kinase activity” (GO:0016301) are found
271 in cluster 2. Preys in this cluster are detected at a higher abundance in T2_NaCl samples. Finally, cluster
272 4 shows enrichment for proteins in the “cytoskeleton” (GO:0005856) and “mRNA 3’-UTR AU-rich region

273 binding" (GO:0035925). Many unanticipated GO terms belong to hyperosmotic stress-specific interactors,
274 highlighting the context-specific nature of the stress granule proximal interaction network.

275 ***B. Quantitative Analysis Shows Context-Specific Rewiring of Proximal Interaction Networks***
276 ***During Stress Granule Assembly and Dissolution.***

277 Using the intensity-based quantitative values measured by DIA analysis, we sought to identify significant
278 changes in the abundance of high-confidence interactors for each bait throughout the stress time course.
279 Quantitative changes in proximal interactions for each bait-prey (e.g., FMR1-BICC1) between all time points
280 (T1 *vs.* T2, T2 *vs.* T3, T1 *vs.* T3) were assessed using a linear mixed model ANOVA with post-hoc pairwise
281 comparisons (Figures 2A, S4B, Methods). We analyzed 22,899 high-confidence bait-prey interactions
282 during oxidative and hyperosmotic stress transitions, respectively (preys identified with BFDR $\leq$ 0.03 in any
283 given time point for each stress condition by one or more baits). Significant changes were identified in 869
284 (3.8%) and 4,881 (21%) bait-prey pairs during oxidative and hyperosmotic stress and recovery transitions,
285 respectively ($\geq$ 1.5-fold intensity change; post-hoc p-value$_{adj}$ $\leq$ 0.01; Table S6). To ensure that the observed
286 changes in the BioID data were not due to global proteome changes during stress, we induced oxidative
287 and hyperosmotic stresses in the G3BP1 Flp-in HEK293 cell line and analyzed the total proteome using
288 the quantitative DIA analysis workflow (see Methods). Differential analysis of global protein abundance
289 revealed minimal changes between no stress and each stress condition, indicating that observed
290 abundance changes are due to proximal interaction changes, not due to proteome abundance changes
291 upon stress (Figure S6A**;** Table S7).

292 Despite the apparent increase in protein concentration within stress granules, contrary to our
293 expectations, high-confidence prey abundance remained largely unchanged following exposure to oxidative
294 stress (T1 to T2; Figure S6B). In contrast, the corresponding distribution tended toward positive fold-change
295 during hyperosmotic stress. Interactions that increased during hyperosmotic stress would later return to no
296 stress-state levels, as indicated by the negative fold-changes observed during the transition from stress to
297 recovery (T2 to T3). These increased interactions during hyperosmotic stress were specific to high-
298 confidence interactors, with the overall intensity of non-significant interactions remaining similar between
299 stress and no stress state (median fold-change for non-significant interactors: 1.05 *vs.* high-confidence

300 interactors: 1.27). This suggests increases in stress granule-specific interactions rather than as a result of
301 general overcrowding in the cytoplasmic space.

302 ***C. Validation of Identified Stress-Specific Interactors***

303 We selected several proteins that increased in a stress-specific manner during stress granule assembly
304 for colocalization analysis with the stress granule marker G3BP1 for validation. TRIM56, BICC1, LARP6,
305 and NYNRIN increased in abundance during oxidative stress, but remained unchanged during
306 hyperosmotic stress. Colocalization analysis was performed under both stress conditions in HeLa cells
307 using antibodies against endogenous proteins or by stable expression of mCherry-tagged proteins. All
308 tested preys localized to stress granules regardless of the inducing agent, except for TRIM56. TRIM56
309 recruitment to stress granules was specific to oxidative stress (Figure S6C; data not shown). BICC1,
310 LARP6, and NYNRIN localized to stress granules during hyperosmotic stress, despite their unchanged
311 abundance measurements. This is not unexpected, as the majority of known stress granule proteins
312 displayed minimal changes in abundance under either stress condition. We further investigated whether
313 TRIM56 plays a role in stress granule assembly. The loss of TRIM56 through CRISPR-mediated knockout
314 did not show defects in stress granule assembly, indicating that increased association with specific
315 components does not entail their essentiality for stress granule assembly (data not shown).

316 Next, we tested if hyperosmotic stress-specific interactors—60S large ribosomal subunits and
317 centrosome-associated proteins—localize to stress granules induced by hyperosmotic stress. When we
318 tested the localization of RPL32 and RPL36 using immunofluorescence microscopy, their cytoplasm-wide
319 diffusive signal made it difficult to assess their colocalization. To reduce their diffusive signal in the
320 cytoplasm, we permeabilized the plasma membrane with a low concentration of digitonin before fixation[83]
321 (see Methods). The digitonin-permeabilized immunofluorescence images showed partial colocalization of
322 G3BP1 with RPL32 or RPL36 subunits in stress granules (Figure S7A-B), consistent with a recent study
323 reporting the presence of 80S ribosomes in stress granules using cryogenic correlative light and electron
324 microscopy[84]. The extent of colocalization between cytoplasmic RPL32 *vs.* G3BP1 or cytoplasmic RPL36
325 *vs.* G3BP1 was consistently the greatest in hyperosmotic stress compared to untreated or oxidative stress
326 conditions (Figure S7C-D), corroborating our stress BioID results. While the trend showed good agreement,
327 the extent of colocalization in hyperosmotic stress was significantly higher than the untreated condition only

328 for RPL36, not for RPL32. As for colocalization analysis of a subset of centrosome-associated proteins
329 (CEP170B, PCNT and CEP192), we found poor enrichment within stress granules during hyperosmotic
330 stress (data not shown). We attribute this to their proximal interactions occurring in the dilute phase.
331 In summary, we validate TRIM56 as an oxidative stress-specific and RPL36, a large ribosomal subunit,
332 as a hyperosmotic stress-specific interactor for stress granules. Further testing is required to elucidate the
333 nature of stress granule interactions with microtubule- and centrosome-associated proteins.
334
335 **Dynamic Proximal Interaction with the CCR4-NOT Complex is Universal during Stress Granule**
336 **Assembly**
337 We hypothesized that quantitative changes across multiple baits and common to both stressors could
338 help identify a shared mechanism underlying stress granule assembly or stress granules' shared function
339 in cellular adaptation to stress. To assess condensate-level changes for each stress, proximal interactions
340 were filtered for those demonstrating consistent trends in their interaction changes (≥ 1.5-fold increase,
341 decrease or unchanged) across two or more baits (Table S6). Consistent changes were observed during
342 hyperosmotic stress (n=564) and oxidative stress (n=68).
343 Next, we assessed shared changes in abundance in both stressors (Figure 2F). While only two high-
344 confidence preys (SUGT, DLD) increased in both oxidative and hyperosmotic stress (≥1.5-fold; ≥2 baits),
345 a significant amount of overlap was observed among interactors that consistently decreased in abundance
346 (30% and 48% of decreasing preys in hyperosmotic and oxidative stress, respectively). These included
347 RNA-binding proteins involved in mRNA deadenylation, translation repression and mRNA decay (*e.g.,*
348 CCR4-NOT complex components and interactors, including TOB1, EIF4E2, and EIF4ENIF1).
349 GO term enrichment analysis of interactors that shift in abundance during stress and recovery (Table
350 S6) identified terms related to 'CCR4-NOT deadenylase complex' among preys that decrease during stress
351 granule assembly and later increase as they disassemble. This trend is consistent across both conditions,
352 as evidenced by the quantitative changes in G3BP1 proximal interactors (Figure S8A). Notably, the
353 decreased association with CCR4-NOT components from T1 to T2 quickly recovers during the T2 to T3
354 transition (Table S6). No changes in total protein abundance of the CCR4-NOT components were observed

355 (Table S7). Together, these observations show the coupling of CCR4-NOT proximal interactions with stress
356 granule assembly dynamics, with no changes in CCR4-NOT abundance.
357
358 **Loss of the CCR4-NOT complex Blocks Lipoamide-induced Inhibition of Stress Granule Assembly.**
359 As stated, pre-treatment with lipoamide effectively inhibits stress granule assembly (Figure 1C). To
360 further characterize this inhibitory pathway and elucidate mechanisms regulating stress granule assembly,
361 we performed a genome-wide CRISPR-Cas9-mediated gene knockout screen (Figure 3A). HeLa cells
362 stably expressing Cas9 and single guide RNAs (sgRNAs) were pre-treated with lipoamide prior to stress
363 with potassium arsenate (As (V)). Confocal images of stress granules, identified by punctate forms of stably
364 expressed FUS-GFP signals, were segmented, quantified, normalized, and transformed into z-scores
365 (Figure 3B; Methods). Notably, the knockout of SRSF1 abolished the inhibitory effects of lipoamide (z-score
366 = 17.5; Figure 3B). This result substantiates the screen, as SRSF1 has previously been shown to prevent
367 lipoamide activity on stress granules[67]. Other gene knockouts (*e.g.,* SLC3A2, ABCC1, large ribosomal
368 subunit proteins, and PPIP5K2) also produced similar inhibitory effects.
369 The microscopy data were manually reviewed, and 81 genes were selected for further validation using
370 endoribonuclease-prepared small interfering RNA (esiRNA)-mediated gene knockdown. Using the same
371 experimental workflow and analysis pipeline as the primary screen, we observed candidates that robustly
372 induced stress granule assembly in cells pre-treated with lipoamide (Figure 3C). Examination of stress
373 granule dynamics in the absence of lipoamide, arsenate (As(V)), or both revealed that the depletion of 22
374 genes induced constitutive stress granule assembly (filled in gray, Figure 3C). These genes, including those
375 that encode helicases, exosome components, ribosome components, and components involved in
376 ribosome biogenesis (RNA polymerase I and WDR43), induced cytosolic FUS-GFP puncta in the absence
377 of cellular stress. Excluding these genes, the depletion of nine others effectively blocked the inhibitory effect
378 of lipoamide on stress granule assembly, including our positive control, SRSF1 (genes in boxes; Figure
379 3C).
380 Among these, GCLC and SLC3A2 are involved in glutathione biosynthesis[85], supporting the redox-
381 associated role of lipoamide for stress granule dynamics[67]. Additionally, the proteasome subunits like
382 PSMA6 and PSMD7 were validated, consistent with prior observations of proteasomal involvement in stress

383 granule dynamics[86]. Notably, PPIP5K2, a bifunctional inositol kinase, and CNOT2, a component of the
384 CCR4-NOT complex, were both identified as high-confidence interactors in the stress BioID data (Table
385 S4).

386 Given the dynamic changes in proximal associations between the CCR4-NOT complex components
387 and stress granule baits, we focused our further investigation on CNOT2. Other CCR4-NOT complex
388 components were depleted to determine whether CNOT2 itself or the complex plays a role in stress granule
389 dynamics. We depleted CCR4-NOT complex components individually or in pairs of the deadenylase
390 paralogs using siRNA (*i.e.,* CNOT7 and CNOT8 or CNOT6 and CNOT6L). Depletion of the NOT module
391 proteins abrogated lipoamide-mediated inhibition of stress granule assembly, whereas depleting the
392 paralog pairs CNOT7-CNOT8 or CNOT6-CNOT6L did not (Figure 3E). Next, we tested removing or
393 depleting deadenylase subunits in different combinations by employing both CRISPR Cas12a knockout
394 and siRNA-mediated knockdown. Removing the CNOT6-CNOT7 pair yielded no suppression of the
395 lipoamide effect, whereas loss of the CNOT6L-CNOT8 pair efficiently blocked lipoamide's effect on stress
396 granules (Figure 3F). Surprisingly, removing all enzymes (CNOT6, CNOT6L, CNOT7, and CNOT8) did not
397 block lipoamide's effect on stress granules, which may be due to the compensatory increase in protein
398 abundance we observed for the remaining subunits. Particularly, the NOT module (CNOT1, 2 and 3)
399 significantly increased in abundance by 1.5~3 fold (Figure S8B). Together, this suggests two possible
400 mechanisms at play in blocking lipoamide's effect: one that depends on the deadenylase activity and
401 another that relies on deadenylase-independent function(s) of the NOT module.

402

403 **Regulation of Poly(A) Tail Lengths is Important for Stress Granule Assembly.**

404 We considered two scenarios in which loss of the CCR4-NOT complex could block lipoamide's effects.
405 First, lipoamide may regulate CCR4-NOT complex function to influence stress granule assembly. However,
406 previous thermal proteome profiling assays using lipoamide showed no change in melting temperature for
407 CCR4-NOT complex components (CNOT1, 2, 3, 4, 6, 7, 10 and 11), advocating against their direct
408 interaction[67].

409 Alternatively, CCR4-NOT may operate in a parallel pathway, distinct from lipoamide regulation, to
410 promote stress granule assembly. Given the established relationship between poly(A) tail length and stress

411 granule assembly [61], and the broader role of mRNAs in condensate assembly [87-91], we hypothesized that
412 poly(A) lengths regulated by the CCR4-NOT complex could modulate stress granule assembly. Longer
413 poly(A) tails may enhance scaffolding for stress granule assembly by providing additional binding sites for
414 poly(A) binding protein (*i.e.,* PABPC1), whereas shorter poly(A) tails could diminish this ability.

415 To assess the influence of poly(A) tail shortening on stress granule assembly, we utilized cordycepin,
416 an adenosine analog that inhibits polyadenylation, to reduce global poly(A) tail length[92]. Cordycepin pre-
417 treatment prior to oxidative stress significantly reduced stress granule and P-body numbers, marked by
418 G3BP1 and DCP1A, in a concentration-dependent manner (Figures 4A-B). PABPC1 recruitment to stress
419 granules was likewise reduced in a dose-dependent fashion, consistent with shorter poly(A) tail diminishing
420 PABPC1-mRNA binding (Figures S8C-D). This can be contrasted with our earlier genetic screens, where
421 inhibiting deadenylase activity by reducing the NOT module of the CCR4-NOT complex positively
422 influenced stress granule assembly. Specifically, in the absence of lipoamide, the knockdown of CNOT1,
423 CNOT2, and CNOT7/8 significantly increased the number of stress granules following oxidative stress
424 (Figure 4C). Together with prior studies reporting global poly(A) tail lengthening following the loss of
425 catalytic enzymes (CNOT7/8) and the NOT module (CNOT1 and CNOT2)[45,93,94], we propose that poly(A)
426 lengthening promotes stress granule assembly.

427 We then combined siRNA-mediated knockdown of the CCR4-NOT complex with cordycepin, lipoamide
428 or both to assess whether poly(A) lengthening can counteract the stress granule-inhibitory effects of these
429 treatments during oxidative stress. While cordycepin pre-treatment alone significantly reduced stress
430 granule assembly, knockdown of CNOT1 prior to acute cordycepin treatment induced stress granule
431 assembly (Figure 4D). This suggests that the stimulatory effects of CCR4-NOT knockdown (*i.e.,* global
432 poly(A) lengthening) can negate the inhibitory effects of acute cordycepin treatment. However, CNOT1
433 knockdown did not overcome the combined inhibitory effects of both lipoamide and cordycepin, leading to
434 defective stress granule assembly. This suggests two parallel pathways regulating stress granule
435 assembly: one through redox regulation of stress granule proteins (via lipoamide) and the other through
436 control of poly(A) tail lengths (via cordycepin and CCR4-NOT activity) (Figure 4E).

437

438 **CCR4-NOT complex is Sequestered to Stress Granules During Stress**

439 Components of the CCR4-NOT have been shown to co-localize with P-body markers in overexpression
440 systems[95,96]. Under endogenous conditions, we observed poor colocalization of CNOT1 with the P-body
441 markers EDC3 (at their endogenous levels) or with DCP1A (stably and inducibly expressed under no stress
442 condition) in HeLa and HEK293 Flp-In T-REx cells (Figures 5A, S9A). However, under both oxidative and
443 hyperosmotic stress, CNOT1 formed large condensates adjacent to P-bodies, similar to the docking
444 behaviour of stress granules[97]. When directly tested, CNOT1 colocalized with stress granule marker G3BP1
445 during both oxidative and hyperosmotic stress in HeLa and HEK293 cells (Figures 5B, S9B). Other CCR4-
446 NOT components, including the NOT module (CNOT2) and the deadenylase subunits, CNOT7 and CNOT8,
447 localized to stress granules under these conditions in HeLa and HEK293 cells (Figures 5B, S9B). Stress-
448 induced localization of CCR4-NOT complex components to stress granules was further confirmed by
449 inducible expression of tagged proteins: 3x-FLAG-CNOT2 in HEK293 and mNeon-tagged CNOT2,
450 CNOT6L, or CNOT7 in HeLa cells expressing mScarlet-G3BP1 (Figures S9C-D). To determine whether
451 the CCR4-NOT complex remains intact during partitioning to stress granules, we visualized CNOT2 BioID
452 interactions with other complex subunits. We observed sustained proximal interactions between CNOT2
453 and the rest of the subunits upon stress, indicating that the complex remains intact in stress granules (Figure
454 5C). Furthermore, high-resolution imaging of CNOT1 and G3BP1 during oxidative stress revealed distinct
455 patterns of CNOT1 enrichment within the G3BP1-positive stress granules, indicating an organized
456 partitioning of the complex into nano-compartments within stress granules (Figure 5D).
457 CNOT1 has been reported as a component of the assemblysomes, formed by translationally inactive
458 ribosome-nascent chain complexes during proteotoxic stress[98]. To distinguish if stress-induced CNOT1
459 puncta are assemblysomes or not, we tested a characteristic that distinguishes the assemblysomes from
460 stress granules and P-bodies: resistance to cycloheximide[99]. Arsenite (As(III)) stress-induced CNOT1
461 puncta colocalizing with G3BP1 dissolved upon cycloheximide treatment, indicating that CNOT1 puncta
462 are not assemblysomes (Figure S10). Together, these findings demonstrate that, endogenous CCR4-NOT
463 complex shows poor P-body localization and the complex is robustly recruited to stress granules during
464 cellular stress.
465

466 **CCR4-NOT Complex Sequestration in Stress Granules Promotes Poly(A) Lengthening of Stress-**
467 **Survival Transcripts.**

468 The CCR4-NOT complex promotes mRNA decay and translation repression via shortening poly(A) tails
469 of transcripts[44,45,100]. To test if stress granule-localization of CCR4-NOT complex was responsible for
470 poly(A) tail lengthening[56-59] observed in stress, we blocked stress granule assembly using lipoamide, and
471 investigated the effect on poly(A) tails and abundance of the transcriptome. We collected total RNAs from
472 HeLa cells under three conditions: no stress, sodium arsenate (20mM As(V)) stress, and lipoamide pre-
473 treatment followed by sodium arsenate stress (200 μM lipoamide + 20mM As(V)) during which lipoamide
474 was sustained (Figure 6A). Lipoamide blocked stress granule assembly and released the CCR4-NOT
475 scaffold protein, CNOT1, back to the cellular environment during cellular stress (Figure S11A). We utilized
476 Nanopore Direct RNA Sequencing (DRS) to determine the poly(A) tail lengths and the abundance of
477 transcriptome in each condition (n=3; see Methods).

478 To examine the effect of stress and blocking stress granules on poly(A) tail lengths, we calculated the
479 average poly(A) tail lengths at the gene level and visualized their distribution. Globally, the average poly(A)
480 lengths minimally changed between no stress and stress conditions. However, lipoamide-mediated
481 inhibition of stress granule assembly reduced the average poly(A) tail lengths compared to the stress
482 condition, which we attribute to the active CCR4-NOT complex that failed to be sequestered to stress
483 granules (Figure 6B). Reduced poly(A) effect is not due to lipoamide agent on its own, as lipoamide
484 treatment in the absence of stress caused a moderate increase in poly(A) tails (Figure S11B).

485 Furthermore, grouping transcripts based on their stress granule localization[30] revealed biases in stress-
486 induced poly(A) tail lengthening. Transcripts enriched in stress granules ('enriched') or neither enriched nor
487 depleted ('neither') showed statistically significant increases in poly(A) length upon stress. These
488 differences suggest that transcripts enriched in stress granules, or neither enriched nor depleted, are more
489 affected by CCR4-NOT's stress granule localization. This corroborates the idea that CCR4-NOT
490 deadenylase activity depends on the translation efficiency of the transcripts[44] ; the complex rapidly
491 deadenylates transcripts with poor translation efficiency, which is a characteristic of stress granule-enriched
492 transcriptome[30]. Regardless of transcript localization, average poly(A) tails were shortened when lipoamide
493 blocked CCR4-NOT sequestration into stress granules compared to the stress condition (Figure 6B).

494 To identify genes significantly regulated by CCR4-NOT complex sequestration to stress granules, we
495 employed the TAILcaller[101], which determines significant poly(A) tail distribution changes in two or more
496 conditions (Figure S11C and Methods). Analyzing reproducible changes in poly(A) lengths between no
497 stress vs. stress (As(V)) or stress (As(V)) vs. lipoamide+stress (As(V)) revealed 374 transcripts and 594
498 transcripts with significant poly(A) length distribution changes, respectively (p_{adj} <0.05 and >|1.3|-fold in
499 median lengths, Figure 6C**,** Table S8). Consistent with the global trend, the majority of transcripts with
500 significant poly(A) tail changes from the no stress to stress comparison showed an increase, while poly(A)
501 tails generally decreased between stress *vs.* lipoamide+stress comparison, reversing the effect of stress
502 on poly(A) tail lengths (Figure 6D). In other words, poly(A) tail lengths in the lipoamide + stress condition
503 were similar to the no stress condition (Figure S11D, left panel).
504 Analysis of significant abundance changes under the same conditions using DESeq2[102] showed the
505 same reversible trend. Pairwise comparisons of no stress vs. stress and stress vs. lipoamide+stress
506 revealed 175 and 165 transcripts, respectively, with significant abundance changes, showing reversal of
507 stress-induced changes in lipoamide+stress condition (Figure 6E). Focusing on stress-induced changes
508 reversed by lipoamide-mediated inhibition, we found a total of 72 transcripts showed significant changes in
509 either direction; 42 significantly increased in abundance upon stress (AsV), which decreased back to the
510 stress level in the lipoamide+stress condition, and 30 showed the opposite trend (Figure 6F).
511 Comparison of transcripts with significant poly(A) tail and abundance changes that are reversed by
512 blocking stress granule assembly identified 15 that are shared, all of whose poly(A) tails and abundance
513 increased upon stress and decreased in the lipoamide+stress condition (Figure 6G). The shared group
514 includes PPP1R15A (GADD34), the regulatory component of the protein phosphatase PP1 complex
515 responsible for inactivating the integrated stress response by dephosphorylating p-eIF2α[103], chaperones
516 (HSPA1A and HSPA1B), and immediate early genes (FOS, FOSB, IER2, JUN and JUNB) activated by the
517 MAPK signaling pathways (ERK1/2, p38 and JNK1)[104], all of which play roles in stress adaptation and
518 promotion of survival (Figure 6G). These genes underlie the specific GO terms observed for this shared
519 group (*e.g.,* genes involved in the regulation of cell cycle and cellular response to oxidative stress; Figure
520 S12A**,** Table S8). Visualizing poly(A) lengths and abundances of individual transcripts in the shared group
521 shows a clear correspondence between poly(A) tails and abundance, which was not seen in the non-

522 significant transcripts (Figure S12B-C). Abundance changes for 4 of the shared group were further validated
523 using RT-qPCR in addition to 6 transcripts showing an opposite pattern (decrease upon stress; Figures
524 S12D-E). Given that these are steady-state measurements, we cannot distinguish if poly(A) lengthening
525 and increased abundance observed in stress-induced survival transcripts reflect reduced decay (*i.e.,*
526 reduced CCR4-NOT activity) or newly synthesized transcripts. Regardless, their stress-induced increase
527 in abundance and extended poly(A) tails depend on the formation of stress granules.

528 Transcripts that showed significant poly(A) tail length changes, but no significant changes in abundance
529 (*i.e.,* poly(A) changes only), were enriched for those regulating transcription by RNA polymerase II, intrinsic
530 apoptotic signaling pathway in response to DNA damage and MAP kinase tyrosine/serine/threonine
531 phosphatase activity (DUSP2 and DUSP5). This suggests that transcripts encoding proteins involved in
532 transcription, apoptosis, and regulation of the MAPK signaling pathway are regulated by stress granule
533 formation via poly(A) tail lengthening. Conversely, transcripts showing significant abundance changes, but
534 no significant poly(A) tail length changes (*i.e.,* abundance changes only), also showed enrichment for
535 transcription-related terms (e.g., DNA-binding transcription factor binding), while showing terms unique to
536 this group, like regulation of cell-cell adhesion. The abundance of these transcripts is likely regulated by
537 post-transcriptional mechanisms other than poly(A) tail lengthening.

538 Together, these analyses uncovered a subset of transcripts encoding proteins involved in stress
539 response or transcription whose poly(A) tail or abundance are regulated by CCR4-NOT sequestration to
540 stress granules.

541

542 **DISCUSSION**

543 Biomolecular condensates participate in a wide range of biological processes, yet their dynamic nature
544 and lack of physical boundaries (unlike membrane organelles) pose significant challenges for study. Stress
545 granules, a condensate formed upon cellular stress, contain thousands of mRNAs and hundreds of
546 proteins[30,31,105]. Despite their widespread association with stress response, the precise functions of stress
547 granules remain controversial. In this study, we leveraged multi-bait BioID profiling and quantitative mass
548 spectrometry to map the dynamic components of stress granules proteomes. Importantly, our approach

549 integrated quantitative protein-protein interaction data with chemical genetic interaction measurements, two
550 orthogonal sources of biological information[106,107], to identify CCR4-NOT complex.

551 BioID profiling of stress granule-localized G3BP1 across a stress time course revealed noticeable
552 changes in proximal interactions accompanying the emergence of microscopically visible stress granules
553 (Figure 1B). Extending this approach to total of nine high-information baits allowed us to define distinct
554 proteomic trajectories of stress granules formed under oxidative versus hyperosmotic stress. These
555 stressors disrupt cellular homeostasis in fundamentally different ways. Oxidative stress generates excess
556 reactive oxygen species that damage macromolecules (*e.g.,* DNA, proteins) and organelles (*e.g.,*
557 endoplasmic reticulum and mitochondria)[73-75], triggering the integrated stress response and stress-
558 activated MAPK signaling pathways, leading to global translation repression, transcriptional reprogramming
559 and metabolic remodeling. In contrast, hyperosmotic stress induces rapid water efflux within seconds,
560 increasing intracellular macromolecular crowding and promoting condensates enriched in WNK kinases,
561 TSC22D and NRBP proteins[77]. Condensate formation, coupled with WNK kinase activation, drives the
562 activation of ion transporters, channels and pumps to restore cell volume through regulatory volume
563 increase[76].

564 Consistent with the distinct cellular challenges posed by these stressors, we observed context-specific
565 proximal interaction networks of stress granules. We uncovered ~2,000 novel proximal interactions—
566 mostly unique to hyperosmotic stress—including many interactions with large ribosomal subunits and
567 cytoskeletal proteins. Immunofluorescence microscopy validation revealed proteins that localize to stress
568 granules in a context-specific manner: TRIM56 upon oxidative stress and a large ribosomal subunit, RPL36,
569 upon hyperosmotic stress (Figures 6C, S7), consistent with our BioID results. We also detected more than
570 500 dynamic protein components (Figure 2F), which differed substantially between stress types, revealing
571 striking plasticity in the stress granule proteome. Despite these differences in protein associations, stress
572 granule transcriptomes are reported to remain highly correlated between oxidative and hyperosmotic
573 stress[108], suggesting that protein dynamics, rather than RNA content, may play a more prominent role in
574 stress-specific adaptations.

575 A shared feature of both stress conditions was the changes in association of the CCR4-NOT complex
576 and its interacting proteins with stress granules (Figure 2F). In parallel, an imaging-based, genome-wide

577 CRISPR screening identified nine genes whose loss suppressed the stress granule-inhibiting effects of
578 lipoamide. These genes include CNOT2, a key component of the CCR4-NOT deadenylases complex
579 (Figure 3D). Loss of any NOT module protein (CNOT1, CNOT2 and CNOT3) or deadenylase subunits
580 (CNOT6L and CNOT8) abolished lipoamide's inhibitory effects (Figures 3E-F). Given that the CCR4-NOT
581 complex is the principal cytoplasmic deadenylase[44-46], we examined whether poly(A) tail length modulates
582 stress granule assembly. Poly(A) shortening inhibited stress granule assembly and PABPC1 recruitment,
583 whereas poly(A) lengthening had the opposite effect (Figures 4B-C, Figures S8C-D). We propose that loss
584 of the NOT module or deadenylase subunits bypasses lipoamide activity either by increasing RNA-based
585 intermolecular interactions[87,88,90,91,105] or providing additional PABPC1 binding sites via poly(A) tail
586 lengthening[61] (Figure 4E). Together, these results reveal a functional link between mRNA deadenylation
587 and stress granule formation.

588 Microscopy-based analysis demonstrated that the CCR4-NOT complex localizes to stress granules
589 during both oxidative and hyperosmotic stress, rather than to P-bodies as previously reported (Figure 5).
590 This was unexpected given the reduced proximal associations detected in BioID experiments (Figure 2F,
591 Figure S8A). We attribute this discrepancy to the *cumulative* nature of BioID experiments, which report the
592 <u>integrated sum of interactions</u> occurring inside and outside stress granules over time. We propose that
593 overall proximity signals decrease during stress either due to reduced transient interactions or due to CCR4-
594 NOT complex partitioning into distinct nanocompartments within stress granules, which would require
595 experimental validations. Additionally, the direction of interaction change depends on the bait used as a
596 probe. We observe increased proximal interactions between the CCR4-NOT complex and other stress
597 granule proteins, PRRC2A and PRRC2B, indicating that the direction of change in bait-specific[109].

598 The discovery of CCR4-NOT localization to stress granules motivated us to investigate whether stress
599 granules contribute to post-transcriptional regulation—a long-standing controversy. Poly(A) tails lengthen
600 during cellular stress[56-59], yet the mechanism has remained unclear. We hypothesized that sequestration
601 of the CCR4-NOT complex into stress granules inhibits its deadenylase activity, thereby driving poly(A)
602 lengthening. Under basal conditions, CCR4-NOT resides in the cytoplasm, not in P-bodies, and modulates
603 transcriptome-wide poly(A) tail lengths, but during stress, it is sequestered into stress granules, away from
604 the translationally active cytosol, where its activity may be regulated.

605 To test this model, we performed global transcriptomics analysis in three conditions: no stress, oxidative
606 stress, and oxidative stress with lipoamide (in which CCR4-NOT remains in the cytosol; Figure 6A).
607 Blocking stress granules and releasing CCR4-NOT during stress resulted in global poly(A) tail shortening,
608 reversing the poly(A) lengthening typically induced by stress (Figure 6B). Despite CCR4-NOT enrichment
609 in stress granules, stress granule-associated transcripts also displayed increased poly(A) tail lengths,
610 supporting that CCR4-NOT activity is inhibited in stress granules.

611 Statistical analysis revealed a subset of transcripts whose poly(A) tail lengths or abundance were
612 significantly regulated by stress granule assembly (Figures 6D and 6F). Stress-induced changes in these
613 transcripts were reversed when stress granule assembly was blocked. Transcripts whose poly(A) tails
614 lengthened in a stress granule-dependent manner were enriched for genes involved in transcription and
615 stress adaptation, including chaperones and components of the MAPK signaling pathway. We propose that
616 CCR4-NOT complex sequestration into stress granules augments the cellular stress response by
617 increasing the levels of key transcripts important for cellular adaptation and survival (Figure 6H).

618 Together, our data support a spatial mechanism by which stress granules remodel post-transcriptional
619 regulation during cellular stress. We show that the CCR4–NOT deadenylase complex is robustly recruited
620 to stress granules, coinciding with poly(A) lengthening and increased abundance of stress-induced survival
621 transcripts. Disruption of stress granule assembly reverses these transcriptomic changes, indicating that
622 condensate formation is necessary for this regulatory switch, likely through CCR4-NOT deadenylase
623 localization. These findings suggest that stress granules function as dynamic sinks that transiently limit
624 cytosolic deadenylation, thereby maintaining elevated levels of stress-induced transcripts available for
625 protein production. Although direct measurements of CCR4-NOT enzymatic activity within stress granules
626 will be required to substantiate this model, the greater extent of poly(A) tail lengthening observed in stress
627 granule-enriched transcriptome supports the possibility that granule-localized CCR4-NOT is functionally
628 attenuated (Figure 6B, H). More broadly, our findings support a model in which biomolecular condensates
629 regulate gene expression not primarily as sites of biochemical activity, but by redistributing limiting
630 regulatory factors in space and time. This work provides a mechanistic framework for understanding how
631 condensate-mediated protein sequestration contributes to adaptive transcriptome remodeling during stress.
632

633 **LIMITATIONS OF THIS STUDY**

634 We report dynamic proximal interaction profiles of multiple stress granule proteins utilized as molecular
635 probes for stress granule condensate. While we are confident of proximal associations reported here, we
636 cannot discern where these proximal interactions occur (*i.e.,* inside or outside microscopically visible stress
637 granules). Furthermore, while we observe clear stress-context dependent heterogeneity in stress granule
638 interaction network, we are unable to test if these interactions occur in stress granules to support structural
639 or functional heterogeneity of stress granules. Thus, further analysis and experimentation are required to
640 determine context-specific stress granule proteome. As with any screening approach, our proteomics and
641 genetic screening methods contain false negatives.

642 With regards to the effect of poly(A) tail lengths affecting stress granule formation, we utilized cordycepin
643 to shorten poly(A) tails globally. Poly(A) tail regulation is a dynamic process, involving both lengthening and
644 shortening. While cordycepin shortens poly(A) tails of the transcriptome globally by terminating RNA
645 synthesis and blocking addition of poly(A) tails [92], it is possible that the concentration used may affect the
646 deadenylation kinetics, as reported in an *in vitro* study[110], which may affect the interpretation of our
647 experiments where we combined cordycepin and CNOT2 knockdown.

648

649 **METHODS**

650 **Cell culture and stable cell line generation**

651 HEK293 Flp-In T-REx (Invitrogen, R780-07; used for fixed-cell microscopy and BioID experiments),
652 HeLa Flp-In T-REx (Arshad Desai Lab), and HeLa (Anne-Claude Gingras Lab) cells were grown at 37ºC in
653 DMEM high glucose media supplemented with 5% Fetal Bovine Serum (FBS), 5% cosmic calf serum, and
654 100 U/mL penicillin/streptomycin (growth media). Cells were regularly passaged upon attaining 80-100%
655 confluency and monitored for mycoplasma contamination.

656 All expression constructs were created using Gateway LR cloning (Thermo Fisher). Entry clones for
657 each bait protein were recombined with a destination vector (pDEST-3xFLAG-miniTurbo for BioID and
658 pDEST-mCherry for microscopy-based assays (gifts from Anne-Claude Gingras, Lunenfeld-Tanenbaum
659 Research Institute) to obtain expression constructs.

660 To generate stable cell lines, our expression constructs were transfected into Flp-In T-REx parental cells
661 following a modified jetPRIME® protocol (Polyplus, CA89129-924). Briefly, cells were seeded at 25-30%
662 confluency in a 6-well plate. The following day, cells were transfected with a mixture of 1 µg pOG44 DNA,
663 100 ng bait construct DNA, and 2 µL jetPRIME reagent in 200 µL jetPRIME buffer (day 2). On day 3, cells
664 were passaged to 10 cm dishes and grown to 80% confluency, where successful transfectants were
665 selected for using Hygromycin B-supplemented growth media (200 µg/mL; Wisent, 450-141-XL) starting on
666 day 4. Selection media was changed every 2-3 days, until clonal colonies were visible; clonal colonies were
667 pooled together to generate stable cell lines.
668
669 **Sample preparation for stress BioID and total proteome analysis**
670 For BioID, we empirically tested 15-minute, 30-minute and 1 h biotin labeling using cells expressing
671 miniT-G3BP1 and found that 30-minute labeling provided optimal balance between obtaining good labeling
672 signal versus capturing dynamic changes. Briefly, HEK293 Flp-In T-REx stable cell lines stably, inducibly
673 expressing BioID constructs, and negative control cell lines (miniT-GFP and HEK293 parental line) were
674 seeded into 10 cm dishes at 30% confluency in 10 mL growth media. After 24 h, protein expression was
675 induced with tetracycline (1 µg/mL) in biotin-depleted growth media for 20 h. Biotin-depleted media is
676 standard growth media prepared with biotin-depleted FBS and cosmic calf serum (as reported in Schreiber
677 *et al.,* 2024[111]). Biotin labeling was then performed for 30 mins using growth media supplemented with 50
678 µM biotin in (1) untreated cells, (2) stress-treated cells, and (3) stress-recovering cells. Stress, recovery,
679 and labelling timelines follow the steps summarized in Figure S2E. For alternative NaCl stress timepoint
680 (T2; 5-35 min), biotin labeling began 5 min into 0.2M NaCl stress for 30min following the same regime as
681 oxidative (As(III)) stress and recovery timepoint (T3; 35-65 min), biotin labeling was performed
682 concomitantly with fresh media change after 35 min of 0.2M NaCl stress (Figure S3B). For global proteome
683 profiling under stress conditions, HEK293 Flp-In T-REx cell lines stable cell lines inducibly expressing
684 miniTurbo-G3BP1 constructs were used. Cells were subjected to (1) no treatment, and (2) stress treatments
685 following the same protocol described above. For lipoamide stress BioID, bait expression was induced for
686 24h in biotin-depleted media. The next day, cells were pre-treated with either DMSO (carrier) or 100 µM
687 lipoamide for 1h prior, then exposed to 1mM or 0mM of potassium arsenate (As(V)) for 1h, after which 50

688 μM biotin was added for 30min of labelling. After labelling, cells were rinsed with phosphate-buffered saline
689 (PBS) and lifted using 0.05% trypsin. Harvested cells were rinsed with PBS, transferred to pre-weighed 1.5
690 mL Eppendorf tubes, pelleted, and flash frozen on dry ice and stored at -80ºC.
691
692 **Generation of Pooled CNOT6L/8 Knockout Cells**
693 Single guide RNAs for CNOT6L and CNOT8 were designed using the CRISPick online tool
694 (https://portals.broadinstitute.org/gppx/crispick/public) with the following settings: Reference Genome =
695 Human GRCh38 (NCBI RefSeq v.GCF_000001405.40-RS_2024_08), Mechanism = CRISPRko, Enzyme
696 = enAsCas12a. A double-stranded geneBlock comprising the CNOT6L and CNOT8 sgRNAs separated by
697 a 20 nt direct repeat sequence and flanked by homology arms (5'-
698 AGGACGAAACACCGGTAATTTCTACTCTTGTAGATGGTGCAGCGCTGTCAAGTGTGTCTAATTTCTAC
699 TATTGTAGATAAAGGTCAACATTGCACCGCAGAAAATTTCTACTCTAGTAGATATAGATCTCCTTGCTA
700 ACTCAGGTAATTTCTACTGTCGTAGATATTTCTATGGTGTTACCTGAAGATTTTTTGAATCTGGTCTTG
701 AAAAAGTGGCACCGAGTCGGTGA-3') was obtained from Integrated DNA Technologies. Three
702 micrograms of the enAsCas12a-encoding vector pRDA-550[112] (a gift from Dr. Diane Haakonsen, Lunenfeld-
703 Tanenbaum Research Institute) was incubated with 10 units of the restriction enzyme Esp3I (New England
704 Biolabs) and 1 unit of recombinant shrimp alkaline phosphatase (New England Biolabs) at 37°C for 2 h and
705 purified by gel extraction. Knockout constructs were generated by Gibson assembly[113] in 20 μL reactions
706 containing 0.02 pmol of digested pRDA-550 vector, 0.06 pmol of the double-stranded sgRNA, 0.08 units of
707 T5 Exonuclease (New England Biolabs), 0.5 units of Phusion DNA Polymerase (New England Biolabs), 80
708 units of Taq DNA Ligase (New England Biolabs), 5% PEG-8000, 100 mM Tris-HCl pH 7.5, 10 mM $MgCl_2$,
709 10 mM dithiothreitol, 1 mM nicotinamide adenine dinucleotide, and 0.2 mM each of dATP, dCTP, dGTP,
710 and dTTP, incubated at 50°C for 1 h. After transforming the reaction into chemically-competent *Escherichia*
711 *coli* NEB10 cells, single clones were selected and validated by sequencing.
712 For knockout cell line generation, HeLa Kyoto cells stably expressing GFP-tagged FUS (FUS-GFP[114])
713 were transfected with a plasmid encoding either EnAsCas12a only or EnAsCas12a plus sgRNAs targeting
714 CNOT6L and CNOT8 using the Lipofectamine 3000 kit transfection protocol (Invitrogen). Cells were

715 selected with 2 μg/mL puromycin after 48 h. A pool of CNOT6L and CNOT8 knockout cells was used for
716 either scrambled or combined esiRNA-mediated knockdown experiments.
717
718 **EsiRNA Knockdown of CNOT 2, 6, and 7**
719 CNOT6L/8 knockout (KO) cells or Cas12a only cells were seeded into 12-well plates onto coverslips at
720 a density of 15,000-20,000 cells/mL. The next day, cells were transfected with esiRNA for CNOT6, CNOT7,
721 CNOT2, or scrambled esiRNA in freshly provided media without antibiotics using Lipofectamine 3000
722 reagent. Briefly, each esiRNA (125 ng) was incubated in Opti-MEM (125 μL) at room temperature for 5 min,
723 alongside a separate mixture of Lipofectamine 3000 reagent (1.25 μL) and Opti-MEM (125 μL) per well.
724 Then, the two mixtures were combined and incubated at room temperature for 20 min. The transfection
725 mixture (250 μL/well) was added to cells, and the media was changed 5 h post-transfection to fresh growth
726 media without antibiotics. The cells were transfected a second time 24 h later, in the same manner as
727 described above. At 24 h post-2nd transfection, the media was refreshed (no antibiotics). After two esiRNA
728 transfections (48 h post 2nd transfection), the cells were then treated with Lipoamide and As(V) in the same
729 manner as described in 'RNA Collection, Processing and Nanopore Direct RNA Sequencing' section. The
730 coverslips were then removed for immunofluorescence analysis, and the remaining cells from untreated
731 samples were harvested for S-Trap sample preparation for total proteome MS analysis and extraction of
732 protein abundance for CCR4-NOT complex components.
733
734 **Puromycin Incorporation Assay**
735 HEK293 Flp-In T-REx cells were plated on a 6-well plate. For each time point, puromycin was incubated
736 for 10 min at a final concentration of 10 μg/mL, as described in Schmidt *et al.*[115]. Cells were either untreated,
737 stressed, or stressed then recovered and puromycin incorporation was performed at indicated condition
738 and timeframes in Figure S2F. Cells were then lifted using trypsin and collected in pre-weighed centrifuge
739 tubes. Cells were normalized by pellet weight and lysed with 2% SDS in Tris-HCl pH 7.5. Samples were
740 boiled with Laemmli sample buffer for 5 min at 95ºC, then analyzed by Western blot (Puromycin Antibody,
741 clone 12D10, Sigma, MABE343).
742

743 **BioID bait selection process**

744 Bait proteins were selected for BioID experimentation by optimizing for the maximum number of
745 theoretical bait-prey interactions using published BirA* BioID data acquired under no stress[63]. We found
746 that 58 baits profiled during no stress showed high specificity in their ability to label and identify literature-
747 curated RNA granule proteins (*i.e.,* ≥70% of their high-confidence interactors are annotated as Tier 1[116]).
748 Using the concepts of the greedy heuristic, we predicted that using five baits (DAZL, YTHDF2, DDX3X,
749 CNOT2, EIF4A2) would recover ~75% of the literature-curated Tier 1 stress granule proteome[116]. The
750 previous study identified stress granule proteins that dually localize to stress granules and other
751 compartments, like P-bodies and nuclear ribonucleoprotein (RNP) complex[63]. To capture components that
752 dynamically transit between stress granules and other RNA-containing compartments, we included CELF1
753 and ZC3HAV1, which identify stress granule proteins and proteins in the nuclear RNP complex or P-bodies,
754 respectively. Next, G3BP1 and FMR1 were added for their importance in stress granule dynamics and
755 translation regulation, respectively. The final list and their relevant selection criteria are summarized in
756 Table S2.

757

758 **BioID sample purification for mass spectrometry**

759 Cell pellets were thawed and resuspended in ice-cold modified RIPA lysis buffer (50 mM Tris-HCl [pH
760 7.5], 150 mM NaCl, 1 mM EGTA, 1.5 mM $MgCl_2$, 1% NP-40, 0.1% SDS) + protease inhibitor cocktail at a
761 1:10 milligram-to-millilitre ratio. Samples were sonicated for 30 s (10 s on, 5 s off, repeat x3) at 30%
762 amplitude using a 1/8" microtip at 4ºC. 250 U of Benzonase Nuclease was added to each sample, which
763 was then rotated end-over-end for 15 min at 4ºC. Sample SDS concentration was raised to 0.4%, then
764 rotated end-over-end for 5 min at 4ºC. Lysate volume was normalized to the lowest weight sample within a
765 bait-stress group, then centrifuged at 20,000 x g for 20 min at 4ºC. Lysates were added to 15 µL of modified
766 RIPA-washed Streptavidin-Sepharose beads of ~60% slurry (Cytiva, 17511301), then rotated end-over-
767 end for 3 h at 4ºC. Beads were pelleted by centrifugation at 500 x g for 1 min, the supernatant aspirated,
768 and the beads transferred to a new 1.5 mL Eppendorf tube using 1 mL modified RIPA buffer. Next, beads
769 were subject to consecutive 1 mL washes (1 x SDS wash (50mM Tris-HCl [pH 7.5]), 2 x modified RIPA
770 washes, 3 x ammonium bicarbonate (ABC) washes (200 mM ABC)), pelleting and aspirating off wash

771 solutions in between. Beads were resuspended in 1 µg trypsin in 30 µL of 50 mM ABC solution for overnight
772 on-bead digestion at 37ºC with agitation. The next day (16 h after trypsin addition), 0.5 µg trypsin in 10 µL
773 of 50 mM ABC was added to each sample, allowing the samples to digest for a further 3.5 h at 37ºC. Beads
774 were pelleted by centrifugation at 400 x g for 2 min, the supernatants containing released peptides were
775 collected into a final collection tube, and the beads were washed with high-performance liquid
776 chromatography (HPLC)-grade water twice, pelleting the beads and collecting the supernatants into the
777 final collection tubes each time. The final collection tubes, carrying the total peptide supernatants, were
778 centrifuged at 16,100 x g for 10 mins, and the top 80 µL was transferred to new tubes, which were acidified
779 to 2% formic acid to stop tryptic digestion and dried down in a centrifugal vacuum concentrator.
780
781 **S-Trap sample preparation for total proteome MS analysis**
782 Protein digestion was performed using S-Trap™ micro spin columns (ProtiFi) following the
783 manufacturer's protocol with minor modifications. Frozen cell pellets were thawed and resuspended in 1X
784 lysis buffer (5% SDS, 50 mM TEAB, pH 8.5) at a ratio of 100 µL buffer per 10 mg pellet. After sonication,
785 samples were centrifuged at 13,000 x g for 8 min, then the supernatant was transferred to a new tube and
786 the protein concentration was measured with a Pierce™ BCA Protein Assay Kit (Thermo Fisher Scientific).
787 For each sample, 50 µg of lysate protein was reduced with 20mM dithiothreitol at 95°C for 10 min, then
788 alkylated with 100 mM iodoacetamide at room temperature for 30 min in the dark. Samples were then
789 acidified with phosphoric acid to pH≤1. Subsequently, 505 µL of binding/wash buffer (100mM TEAB in 90%
790 methanol) was added to the solution. This mixture was loaded onto S-Trap micro spin columns and
791 centrifuged at 4,000 × g for 30 s to trap proteins. Following the first centrifugation, washing was repeated
792 four times by adding 150 µL of binding/wash buffer and centrifuged at 4000 × g for 30 s. The final column
793 spin was conducted at 4000 × g for 1 min to fully remove binding/wash buffer.
794 Next, 20 µL of trypsin (~1:10 enzyme/protein) in digestion buffer (50 mM TEAB) was added to the
795 surface of the filter and incubated for 2 h at 47°C. The tryptic peptides were eluted sequentially with 40 µL
796 each of (1) 50 mM TEAB, (2) 0.2% formic acid, and (3) 50% acetonitrile via centrifugation for 1 min at 4000
797 × g. Eluted solutions were pooled together and the final peptide concentration was measured with a

798 colorimetric Pierce™ Quantitative Peptide Assay Kit (Thermo Fisher Scientific). Eluates were dried down
799 via vacuum centrifugation and stored at −80°C.
800
801 **Liquid Chromatography-Mass Spectrometry**
802 BioID peptides were resuspended in 12 µL of 5% formic acid and centrifuged at >20,000 x g for 1 min.
803 For MS analysis of BioID peptides, each sample was further normalized to the smallest pellet weight across
804 all bait-stress groups by diluting ~1-2 µL of the peptide solution with 5% formic acid to a volume of 12 µL.
805 Subsequently, 1 µL of 50 fmol/mL Pierce Retention Time Calibration (iRT) peptides was added, bringing
806 the final volume to 13 µL. For MS analysis of total proteome samples, peptides were resuspended in 5%
807 formic acid to 200 ng/µL, and 1 µg of peptide suspension was combined with 1 µL of 50 fmol/mL Pierce iRT
808 peptides in a total volume of 13 µL.
809 For each sample, 6 µL of peptides was loaded onto a 10.5 cm 75 µm ID emitter tip packed in-house with
810 3 µm ReproSil Gold 120 C18 (Dr. Maisch HPLC GmbH) using an Easy-nLC 1200 liquid chromatography
811 system. Peptides were eluted at 200 nL/min over a 120 min gradient, starting with 2.4% acetonitrile in 0.1%
812 formic acid and gradually increasing to 35% acetonitrile. The acetonitrile concentration was further
813 increased to 80% over an 8 min gradient and maintained at this concentration for 16 min at 200 nL/min, for
814 a total run time of 144 min. Samples were analyzed with an Orbitrap Exploris 480 (Thermo Fisher Scientific)
815 in both Data-Independent Acquisition and Data-Dependent Acquisition modes. Instrument configurations
816 for both acquisition modes were set up using Thermo Xcalibur (V4.6.67.17) software. The instrument was
817 operated with a positive polarity ion voltage of 2.4 kV and the ion transfer tube temperature was set to
818 300°C. MS analyses of each BioID sample was done in both DIA and DDA modes consecutively, while the
819 fractionated HEK293 peptides were analyzed in DDA mode only.
820 For DDA experiments, MS1 scans ranged from 390-1010 m/z were performed at a resolution of 120,000,
821 with a 3-second cycle time. The normalized automatic gain control (AGC) target was set to 125%. Precursor
822 ions with charges from 2+ to 7+ that exceeded an intensity threshold of 1.0×10^3 were selected for
823 fragmentation with dynamic exclusion enabled for 9 seconds. Fragmentation was achieved with a
824 normalized collision energy (NCE) of 33%. MS2 scans were performed at a resolution of 15,000, with a

825 normalized AGC target of 400%, and a maximum injection time of 50 ms. The DDA-MS data were used to
826 generate spectral library for DIA deconvolution and benchmark BioID-DIA analysis workflow.
827 For DIA experiments, a staggered window scheme was utilized as described in Pino et al., 2020[117].
828 Briefly, this approach employed two alternating precursor isolation patterns with the m/z ranges of 400-
829 1,000 and 396-1,004 m/z, respectively. MS1 scans were acquired in centroid mode at a resolution of
830 60,000, a normalized AGC target of 100%, a maximum injection time of 55 ms and a scan range of 390-
831 1,010 m/z. MS2 scans were acquired in a DIA window scheme consisting of 75 and 76 8m/z isolation
832 windows, at a 15,000 resolution, with a scan range of 145-1450 m/z, a normalized AGCw target of 1000%,
833 a maximum injection time of 23 ms and normalized collision energy of 33%.
834 The Gas Phase Fractionation (GPF) approach was chosen over the DDA-based library generation for a
835 subset of experiments because it reduced the time and effort required. To generate a spectral library for
836 the analysis of global proteome changes under stress, six GPF acquisitions were acquired from a pooled
837 biological sample pool from HEK293 cells (2 µL each from 15 total proteome samples). The GPF acquisition
838 scheme utilized was described in detail in Pino et al., 2020[117]. Each GPF injection was acquired at a MS1
839 resolution of 60,000 and MS2 resolution of 30,000, with an AGC target of 1000%, maximum injection time
840 of 55 ms, and normalized collision energy of 33%. Precursor ions were isolated using staggered 4 m/z
841 windows. Each of the six injections covers a distinct m/z range: 398–502, 498–602, 598–702, 698–802,
842 798–902, and 898–1002.
843
844 **Mass Spectrometry Data Analysis: Data-Dependent Acquisition and Gas Phase Fractionation**
845 All MS files acquired in DDA and GPF modes were analyzed separately with FragPipe (v20.0),
846 MSFragger(v3.8)[118], IonQuant (v1.9.8)[119] and Philosopher (v5.0.0)[120]. For GPF data, Thermo RAW files
847 were first computationally demultiplexed and converted to mzML format prior to analysis (see
848 **Demultiplexing of DIA staggered windows**). The protein sequence database contains reviewed UniProt
849 entries and 15 iRT peptides as well as the same number of reversed decoy sequences, with a total search
850 space of 40,884 sequences. The precursor mass window was set at ±20ppm and the fragment mass
851 tolerance was set at ±20ppm. Tryptic digestion was specified with full enzyme specificity, allowing up to two
852 missed cleavages. Methionine oxidation (+15.9949 Da), and N-terminal acetylation (+42.0106 Da) were set

853 as variable modifications, while carbamidomethylation of cysteine (+57.0215 Da) was set as a fixed
854 modification. For BioID samples, carbamidomethylation of cysteine (+57.0215 Da) fixed modification was
855 omitted, as alkylation step is not included in BioID processing steps. Additionally, peptide N-terminus heavy
856 arginine (+10.008269) and heavy lysine (+8.014199) were included as variable modifications to facilitate
857 the identification of iRT peptides. The GPF data search also included lysine biotinylation (+226.07760) as
858 a variable modification. MSBooster was enabled, which uses deep learning to predict retention time and
859 spectra to increase identifications[121]. PSM validation was done using Percolator (--only-psm --no-terminate
860 --post-processing-tdc), which uses a linear support vector to performs FDR calculations using a target-
861 decoy approach[122]. This is followed by protein inference by ProteinProphet (--maxppmdiff 20)[123]. FDR
862 filtering was done using Philosopher to 1% PSM and protein levels (--sequential --picked --prot 0.01).
863 MS1 intensity-based quantification was conducted using IonQuant with Match-Between-Runs (MBR)
864 enabled (default parameters)[119,124]. MaxLFQ intensity (with minimum ions set to 2) was used for
865 downstream statistical analysis. For feature detection and peak tracing, m/z tolerance was set to 10ppm
866 and RT Window to 0.6. MBR top runs was set to 10.
867
868 **Spectral Library Generation**
869 Two spectral libraries were generated for DIA data analysis: (1) DDA-based library used for the analysis
870 of BioID data and (2) GPF-based library for global proteome analysis. For the first library, the DDA search
871 results from fractionated peptides of HEK293 lysate and BioID peptides were compiled into a spectral library
872 using EasyPQP with default parameters (v0.1.42) (https://github.com/grosenberger/easypqp). The initial
873 library file then underwent a 3-step filtering process to generate the final library in TSV format. First,
874 precursors containing alkylated cysteine residues were filtered out to minimize false positives because
875 cysteine reduction and alkylation is not performed during BioID sample processing. Second, fragments
876 outside the 350-2000 m/z range were removed as signals outside this range are typically noisy. Finally, the
877 six most intense fragments for each precursor were retained, and precursors with less than six fragments
878 were excluded[125]. Using a defined number of fragments in the library ensures uniform statistical distributions
879 during automated peak scoring in DIA analysis (i.e., different numbers of fragments per precursor may

880 result in mixed statistical distributions for the target identifications). The final DDA-based spectral library
881 contains 193,510 precursors from 9,860 proteins.
882 The generation of GPF-based library used the same workflow applied to the GPF search results. In this
883 case, alkylated cysteine filtering was omitted, as the total proteome samples were reduced with
884 iodoacetamide. The GPF-based spectral library contains 44,887 precursors from 37,204 peptides and
885 5,203 proteins.
886
887 **Demultiplexing of DIA staggered windows**
888 DIA and GPF-MS data acquired using the staggered window scheme require a computational
889 demultiplexing step before they can be processed by data analysis software. This step resolves the
890 staggered precursor isolation windows into effective windows that are halves of the original width. For
891 example, 8 m/z staggered windows spanning m/z range of 400-100m/z would be demultiplexed into non-
892 overlapping 4m/z windows: 400–404 m/z, 404–408 m/z, 408–412 m/z, etc. The demultiplexing was
893 performed by MSConvert (ProteoWizard) with the following filters: 1) ”peakpicking vendor msLevel=1-“; 2)
894 “demultiplex optimization=overlap_only massError=10.0ppm”. The resulting mzML files are used for
895 downstream data analysis
896
897 **Mass Spectrometry Data Analysis: Data-Independent Acquisition**
898 The DIA-MS data in mzML format were analyzed by the DIA-NN software (v1.8.1)[81] using a library-
899 based approach. BioID and global proteome data were analyzed separately. The BioID and CNOT KD total
900 proteome data were searched against the DDA-based spectral library described above (see **Spectral**
901 **Library Generation**), while analysis of the stress total proteome data utilized the GPF-based spectral
902 library. DIA-NN was configured with match-between-runs enabled, cross-run normalization and MaxLFQ-
903 based protein quantification disabled. Mass accuracy was set to 20 ppm for both MS1 and MS2.
904 Additionally, the *“--report-lib-info*” flag was set to generate fragment-level intensity values in the resulting
905 report.tsv file, which was used for downstream statistical analysis. The resulting DIA-NN report.tsv file was
906 first filtered using global precursor and protein FDR thresholds of 1% (Lib.Q.Value ≤ 1% and

907 Lib.PG.Q.Value ≤ 1%) to ensure high-confidence identifications. Fragment-level (MS2) intensity data were
908 extracted from the "Fragment.Quant.Raw" column in the report.tsv.
909 For BioID data, intensity normalization was then performed within each bait group by scaling fragment
910 intensities to a common total MS2 intensity. Specifically, the intensity value of each fragment in a sample
911 is divided by the sum of total fragment intensities in the sample and multiplied by the median of the sum of
912 fragment intensities across all samples in a bait or control group. The resulting normalized fragment
913 intensity matrix was used for SAINTq (V0.0.4)[82] analysis to identify high-confidence interactors and for
914 Mixed-Model ANOVA to identify dynamically associating interactors (see Data Analysis). For global
915 proteome data, intensity normalization was performed by adjusting for total MS2 intensity across all
916 samples prior to mixed-model ANOVA to identify differentially abundant proteins.
917
918 **Mass Spectrometry Data Deposition**
919 Datasets consisting of raw files and associated peak list and results files have been deposited in
920 ProteomeXchange through partner MassIVE as complete (Data Dependent Acquisition) or partial (Data
921 Independent Acquisition) submissions. Additional files include the complete SAINTexpress (V3.6.3) outputs
922 for each dataset and a "README" file that describes the dataset composition and the experimental
923 procedures associated with each submission. The DDA and DIA datasets generated here were each
924 submitted as independent entries. The accession numbers for the DDA dataset are MSV000095953
925 (ftp://massive.ucsd.edu/v08/MSV000095953/) in MassIVE and PXD056247 in ProteomeXchange. The
926 accession number for the DIA dataset is MSV000095944 (ftp://massive.ucsd.edu/v08/MSV000095944/).
927 The accession number for the total proteome DIA dataset including GFP-DIA data used to generate spectral
928 library is MSV000098662 (ftp://massive-ftp.ucsd.edu/v10/MSV000098662/). Total proteome data for cell
929 lines with knockouts and/or knockdowns of CCR4-NOT components were deposited with the MassIVE ID
930 MSV000100193 (ftp://massive-ftp.ucsd.edu/v11/MSV000100193/).
931
932 **Data Analysis: SAINTexpress and SAINTq to Identify Confident Interactors**
933 Significance Analysis of INTeractome (SAINT) comprises a series of computational tools used to assign
934 confidence scores to protein-protein interaction based on quantitative data generated from AP-MS and

935 BioID experiments[65]. Recent versions of SAINT have been extended to analyze intensity-based data[66,82,126],
936 with SAINTq implemented specifically for the analysis of intensity data at the protein, peptide and fragment
937 levels[82]. Although SAINTq has been available since 2015, its application in BioID projects has not been
938 widely tested. We generated BioID-SAINTq analysis pipeline for protein- and fragment-level intensity data
939 and benchmarked it against the established BioID-SAINTexpress.

940 *SAINTexpress Workflow:*

941 Spectral-count based analysis of DDA BioID data was performing using SAINTexpress as
942 implemented within the Fragpipe framework. The "reprint.spc.tsv" was the input for SAINTexpress and the
943 analysis was performed using the default parameters. Identified prey proteins with BFDR $\leq$ 0.05 are
944 considered high-confidence interactors.

945 *SAINTq Workflow:*

946 For DDA protein-level intensity-based analysis used for internal quality control, we used the
947 "combined_protein.tsv" file generated by Fragpipe. After selecting the MaxLFQ intensity columns, the data
948 were normalized by total intensity within each bait group before running a modified version SAINTq (v0.0.4),
949 provided by the Anne-Claude Gingras Lab
950 (https://github.com/vesalkasmaeifar/Modified_SAINTq_and_SAINTexpress). For DIA fragment-level
951 intensity-based analysis, the total intensity normalized fragment matrix (see Mass Spectrometry Data
952 Analysis: Data-Independent Acquisition) was analyzed by SAINTq. In both DDA and DIA SAINTq analyses,
953 control compression was disabled and default parameters were applied. Using the benchmark of known
954 stress granule proteome and results from DDA SAINTexpress, we have manually assigned BFDR 0.03 as
955 a suitable threshold for high-confidence interaction.

956

957 **Data Analysis: Unsupervised Hierarchical Clustering and Data Visualization**

958 To ensure the quality of DIA proteomics data prior to unsupervised hierarchical clustering, we applied a
959 two-step filtering process to each bait group. First, fragments missing in more than 80% of samples within
960 a group were excluded from the analysis. Second, precursors with fewer than three fragments were filtered
961 out. These filters were applied because fragments or precursors not quantified in the majority of samples

962 are likely noises. Next, protein intensity values were rolled up by summing intensities of corresponding
963 fragments and the resulting intensity values were log2-transformed.
964 To infer proximal interactions associated with the stress granule condensate rather than bait-specific
965 interactions, we filtered for 1,801 high-confidence interactors (BFDR ≤ 3%, SAINTq) that were identified by
966 at least two baits, regardless of the condition. We assumed that high-confidence interactors identified
967 across multiple baits are more likely to be associated with stress granules.
968 Clusterings of bait-conditions (columns) and proteins (rows) was performed using Euclidean distance
969 and Ward's method for linkage. The R package pheatmap was utilized for heatmap visualization. To
970 determine the most informative number of clusters for protein groupings, we computed the within-cluster
971 sum of squares (WCSS) across a range of cluster numbers. WCSS measures the total variance within each
972 cluster by summing the squared distances between each protein and the average profile of its assigned
973 cluster. A lower WCSS value indicates more compact and coherent groupings, reflecting similar abundance
974 patterns across samples. An elbow plot was generated to visualize the change in total WCSS as the number
975 of clusters increased. The optimal number of clusters was selected at the point where the curve plateaued.
976 Based on this approach, four clusters were identified as the most informative. Finally, gene ontology (GO)
977 enrichment analyses were performed for proteins in the four-row clusters using g:Profiler. The background
978 protein set for the GO enrichment analysis consisted of 9,860 protein entries in the spectral library, as these
979 represent the proteins detectable in the experiments. GO terms with FDR ≤ 1% (Benjamini-Hochberg) are
980 significant.
981
982 **Data analysis: Mixed-Model Analysis of Variance**
983 The total intensity normalized fragment matrix contained a sizable proportion of missing values. To
984 improve statistical power, the matrix was imputed using a K-Nearest Neighbor (KNN) approach using the
985 python package scipy (V1.10.1), with the number of neighbors (k) set to 5. We then used the filtered proteins
986 from two-step filtering process (see Data Analysis: Unsupervised Hierarchical Clustering and Data
987 Visualization), to select for high-quality fragments. Next, precursor intensity values were rolled up by
988 summing intensities of corresponding fragments and the resulting intensity values were log2-transformed.

989 A linear mixed model was then applied to the KNN-imputed, log_2-transformed precursor intensity matrix.
990 This model was used separately to the BioID and global proteome datasets to assess prey protein dynamics
991 across time points for each bait (**T1 vs T2_As(III) vs T3_As and T1 vs T2_NaCl vs T3_NaCl**), and to
992 evaluate global proteome changes in response to stress (**T1 vs T2_As(III) vs T2_NaCl**), respectively.
993 The linear mixed model is defined as:

994 $$Intensity_{ij} = \beta_0 + \beta_1 \cdot Timepoint_i + u_j + \epsilon_{ij}$$

995 where $Intensity_{ij}$ represent log2-transformed intensity for precursor j at time point i. β_0 is the overall
996 intercept, β_1 is the fixed effect coefficient representing the effect of time point i, u_j is the random effect
997 accounting for variability among different precursors, and ϵ_{ij} is the residual error term. This model accounts
998 for the random effect of the precursors corresponding to the same protein and the fixed effect of the
999 timepoint. In cases where only a single precursor is available, a simpler linear model is applied without the
1000 random effect:

1001 $$Intensity_i = \beta_0 + \beta_1 \cdot Timepoint_i + \epsilon_i$$

1002 Analysis of variance (ANOVA) was then applied to obtain p-values indicating the significance of time point
1003 effects. Post-hoc analysis was conducted using estimated marginal means to evaluate pairwise fold change
1004 between time points (i.e T1 vs T2_As(III)). The Benjamini-Hochberg procedure was applied to correct for
1005 multiple comparisons, with differential interactions defined by p-adjusted values ≤ 0.01 and fold change ≥
1006 1.5.
1007

1008 **Immunofluorescence (IF) microscopy**

1009 For bait localization and prey colocalization tests, stable HEK293 or HeLa Flp-In T-REx BioID cell lines
1010 were seeded onto glass coverslips in 6-well plates at 20% confluency in 2 mL growth media, and protein
1011 expression was induced 24 h later with tetracycline (1 µg/mL) for 20 h. For lipoamide titration tests, HEK293
1012 BioID stable cells stably expressing miniT-G3BP1 or miniT-GFP were seeded at 30% confluency, then
1013 induced for bait expression for 24 h. Varying concentrations of lipoamide (0-100 µM) or carrier (DMSO)
1014 were added, followed by no treatment (untreated) or potassium arsenate (As(V)) stress (1 – 2 mM). For
1015 stress granule assembly assays in cordycepin treatment (Figure 4A-B), HEK293 Flp-In T-REx, HeLa Flp-
1016 In T-REx, or HeLa cells were seeded onto glass coverslips in growth media. Glass coverslips were treated

1017 with poly-D-lysine for 1 h at 37ºC prior to seeding HEK293 Flp-In T-REx cells. Cells reached 90% confluency
1018 24-48 h post seeding onto the glass coverslips and were treated with either a media change (untreated),
1019 sodium arsenite (III) [60 μM – 1 h, 75 μM – 1 h, 500 μM – 30 min], sodium chloride [0.2 M – 1 h], or sorbitol
1020 [sorb: 0.4 M, 1 h]) at 37ºC.

1021 To detect colocalization of 60S subunits (RPL32 and RPL36) with stress granules in Figure S7, HeLa
1022 cells were treated with either sodium arsenite (III) (0.5mM) or sodium chloride (0.2M) for 30 min, washed
1023 once with ice-cold PBS, then incubated twice with 0.01% digitonin in PBS on ice for 2 min. After the second
1024 incubation, the digitonin was aspirated, and the cells were fixed and processed for IF processing steps
1025 below. For the cordycepin treatment in Figures 4A-B and S8C-D, cells were pretreated with varying
1026 concentrations of cordycepin [0-100 μM; C3394, Sigma-Aldrich] for 3 h, with varying amounts of sodium
1027 arsenite (III) added during the last h before fixation. For the cordycepin treatment in Figure 4D, the HeLa
1028 Kyoto FUS-GFP cells (MCB_005340) were first treated with the indicated concentration of cordycepin
1029 (C2689, Tokyo Chemical Industry) for 1 h, then treated with 10 μM of lipoamide or the corresponding
1030 percentage (v/v) of DMSO (0.1%) as the control for 1 h, and finally stressed with 1 mM of potassium
1031 arsenate (As(V)) for 1 h before fixation with 4% formaldehyde in PBS.

1032 Cells were processed for IF immediately following drug treatments by rinsing the cells with PBS twice,
1033 then fixing with 4% paraformaldehyde in PBS for 10-15 min. Post fixation, cells were washed 3 times with
1034 PBS or TBS-T and then permeabilized with -20ºC methanol (Figure 4A, 5, S2B, S7A-B, S8, S9A-B, S10,
1035 S11A) or 0.1% Triton-X in TBS-T (Figure S1B, S2A, S2C, S2D, S6C, S9C-D) at room temperature for 10
1036 min. Cells were then washed 3 times with PBS or TBS-T, then blocked with 5% milk in TBS-T or 5% BSA
1037 in PBS for 1 h. Coverslips were then incubated in primary antibody solution prepared in 5% BSA in PBS for
1038 1 h or overnight (depending on the antibody) in a humidity chamber at 4ºC. The cells were then washed 3
1039 times with PBS or TBS-T and then incubated with secondary antibodies and DAPI prepared in 5% BSA or
1040 milk blocking solution for 1 h in the dark. Coverslips were then washed for 3 times with PBS or TBS-T.
1041 Finally, samples were mounted onto slides using Prolong Gold and cured in the dark overnight. All steps
1042 were performed at room temperature, excluding the overnight incubation. Samples were imaged using the
1043 Leica SP8 Confocal Microscope and the Leica Stellaris 5 Confocal Microscope at 40X and/or 63X

1044 magnification using LASX (V3.5.7.23225 and 4.7.0.28176), and images were processed using either
1045 IMARIS (V10.1.1) or LASX software (4.8.0.28989).
1046
1047 **High Content Genetic Screen of Lipoamide**
1048 To generate a cell line stably expressing Cas9 and GFP-tagged FUS, A plasmid of human codon-
1049 optimized *S. pyogenes* Cas9 (lentiCas9-Blast; #52962, Addgene) was transfected into HeLa Kyoto cells
1050 stably expressing FUS-GFP[114] (MCB_005340), and the clone was selected with 20 µg/mL of blasticidin.
1051 The obtained clone cells were seeded at 550 cells/well in 384-well plates (#781092, Greiner),
1052 transfected with 20 nM each of tracrRNA (U-002005, Horizon) and sgRNA from Human Edit-R crRNA
1053 library (18,710 genes tested; Dharmacon) using Interferin (polyplus), and incubated for two days before the
1054 medium was replaced with fresh one for 1 day. CRISPR-Cas9-mediated gene knockout was validated with
1055 KIF11 sgRNA, which kills cells. An sgRNA targeting SRSF1 (CM-018672-01, Horizon) was used to validate
1056 the assay. Mock transfection was used for controls both positive and negative for stress granule assembly.
1057 Three days after transfection, the cells were pre-treated with 20 µM of lipoamide for 1 h and then stressed
1058 with 1 mM of potassium arsenate (As(V), A6631, Sigma Aldrich) for additional 1 h in the presence of
1059 lipoamide before fixed with 4% formaldehyde in PBS. For only mock transfection, wells without lipoamide
1060 treatment were also prepared for the positive control. The fixed cells were stained with 1 µg/mL of DAPI
1061 and 0.25 µg/mL of CellMask blue (H32720, Thermo Fisher Scientific) and imaged on a CellVoyager CV7000
1062 (R1.17.05) automated spinning disc confocal microscope (Yokogawa) with a 40× NA 1.3 water objective
1063 lens.
1064 For the secondary screen, the HeLa Kyoto FUS-GFP cells were seeded at 1000 cells/well in 96-well
1065 plates (#655090, Greiner), transfected with 25 ng of each endoribonuclease-prepared small interfering RNA
1066 (esiRNA; Eupheria) using Lipofectamine2000 (Invitrogen). Three days after transfection, the cells were
1067 treated with 10 µM of lipoamide for 1 h and then stressed with 1 mM of potassium arsenate (As(V)) in the
1068 presence of lipoamide for 1 h before fixed with 4% formaldehyde in PBS. The cells were stained with
1069 1 µg/mL of DAPI and imaged similarly to the primary screen.
1070
1071 **Confocal Image Analysis**

1072 For high content imaging analysis (relevant to Figures 3B-E and 4C-D), segmentation of stress granules
1073 were performed based on cytoplasmic FUS-GFP signals using CellProfiler (V4.2.4)[127], and the obtained
1074 information (*e.g.*, number and size of stress granules, intensity of FUS-GFP) was processed with KNIME
1075 (V4.7.0) and Fiji (V2.16.0). For primary genome-wide CRISPR screen, the number of stress granules per
1076 cell treated with each sgRNA was normalized relative to two datasets: that of mock transfection without
1077 lipoamide treatment (defined as 100%) and that of mock transfection with lipoamide treatment (0%) within
1078 each plate; the normalized values were transformed into z-scores as shown in Figure 3. For the
1079 quantification of immunofluorescence images (relevant to Figure 4A-B), segmentation and quantification
1080 were performed using CellProfiler (V3.0). Manual quantification of immunofluorescence images shown in
1081 Figure 3F was done using Fiji (V2.14.0). All of the images were processed together to avoid bias during
1082 quantification. Any cells with ≥3 FUS-GFP positive puncta in the cytoplasm were counted as a stress
1083 granule-positive cell.
1084 For colocalization analysis between large ribosomal subunits (RPL32 and RPL36) in Figure S7,
1085 CellProfiler Version 4.2.8 was used. First, the nucleus was segmented with the 'IdentifyPrimaryObjects'
1086 using DAPI. Then, the nucleus was masked in the RPL channel to exclude the nuclear signal from analysis.
1087 Colocalization measurements across the entire image were performed for the masked RPL channel and
1088 G3BP1 channel using the MeasureColocalization module.
1089

1090 **Cyclohexamide Treatment**

1091 HeLa Flp-In cells were seeded onto coverslips in a 12-well plate with 1.5 $X10^5$ cells. The following day,
1092 the cells were stressed with sodium arsenite (III) at a concentration of 60 μM. After 1 h of stress, either
1093 ethanol (carrier) or cyclohexamide (10 μg/mL final concentration) was added via spike-in for both 30 and
1094 60 min. Cells were then processed following the IF protocol listed above.
1095

1096 **RNA Collection, Processing and Nanopore Direct RNA Sequencing**

1097 The following steps were applied to three biological replicates. HeLa Flp-In cells were seeded into 6cm
1098 dishes with $1X10^6$ cells, including and matching samples at the same relative density onto coverslips in a
1099 12-well plate for IF. The next day, the cells received a fresh media change 1 h prior to adding lipoamide.

1100 Lipoamide (in DMSO) was added to the cells via media change at a concentration of 200 μM. DMSO was
1101 added as a carrier to the no-stress and sodium arsenate (As(V)) conditions. After 1 h of lipoamide, cells
1102 were stressed with arsenate (As(V) in water) via spike-in at a final concentration of 20mM. One hour after
1103 As(V) was added, the cells were collected simultaneously for IF and RNA extraction. The IF was processed
1104 as described above. The samples for RNA were washed quickly with PBS twice, then lysed with 600 μL Tri
1105 Reagent per 6 cm dish for 5 min with rocking. Samples were moved to a Lo-Bind microfuge tube on ice,
1106 and 120 μL chloroform was added to the samples. Samples were shaken vigorously 20 times and incubated
1107 on ice for 15 min. Samples were then centrifuged at 4°C for 15 min at 12,000 rpm, and the aqueous (top)
1108 layer (~300 μL) was carefully removed and placed into a new Lo-Bind tube on ice. Following this, 300 μL
1109 of isopropanol was added to the samples, and they were shaken vigorously 20 times and incubated
1110 overnight at -20°C. The next day samples were spun at 4°C for 15 min at 12,000 rpm. The isopropanol was
1111 carefully removed, leaving a small pellet. The pellets were washed with 1 mL of ice-cold 100% ethanol and
1112 vigorously shaken 20 times. The samples were spun again at 4°C for 10 min at 12,000 rpm. The ethanol
1113 was carefully removed, and the pellet was left to dry at room temperature. Once dry the RNA pellet was
1114 resuspended with 50 μL of nuclease-free water and concentration was checked with a Biotek Epoch reader.
1115 To prepare the RNA samples for subsequent analysis, 10 μg of RNA was digested with TURBO DNase
1116 following the manufacturer's protocol (30 min at 37°C). The RNA samples were then cleaned up with the
1117 Qiagen MinElute Column Clean-up Kit (Cat. 74204) following the manufacturer's protocol for Nanopore
1118 Direct RNA Sequencing or RT-qPCR.
1119 Direct RNA sequencing was performed by The Centre for Applied Genomics at The Hospital for Sick
1120 Children, Toronto, Canada. RNA concentration and integrity were assessed using the Qubit™ RNA HS
1121 Assay Kit (ThermoFisher, Q32852) and by the Bioanalyzer RNA 6000 Nano assay (Agilent, 5067-1511).
1122 Library preparation was performed using the Direct RNA Sequencing Kit (Oxford Nanopore Technologies,
1123 SQK-RNA004) following the manufacturer's protocol version 9195_v4_revB_20Sep2023. Briefly, 1 μg of
1124 total RNA in 8 μl nuclease-free water was used as input. Prior to reverse transcription, 25ng of
1125 *Saccharomyces cerevisiae* RNA for ENO2 was spiked into the RNA samples used for sequencing validation
1126 of ONT transcripts. Reverse transcription adapter (RTA) was ligated to the RNA using T4 DNA Ligase
1127 (NEB, M0202M) and NEBNext® Quick Ligation Reaction Buffer (NEB, B6058), followed by reverse

1128 transcription using SuperScript™ III Reverse Transcriptase (Thermo Fisher Scientific, 18080044) to
1129 synthesize a complementary cDNA strand for stability. The cDNA strand was not sequenced. Post-reverse
1130 transcription, the RNA-cDNA hybrid was purified using Agencourt RNAClean XP beads (Beckman Coulter,
1131 A63987). Sequencing adapters were then ligated to the hybrid using T4 DNA Ligase and RNA Ligation
1132 Adapter (RLA), followed by another bead-based purification step. The final library was quantified using the
1133 Qubit™ dsDNA HS Assay Kit (ThermoFisher, Q32851), and the entire volume was used for sequencing.
1134 The final libraries were sequenced on the Promethion-24 instrument (Oxford Nanopore Technologies) on
1135 FLO-PRO004RA flow cells for a 90-96 h run. Basecalling was performed with the High-accuracy model
1136 (HAC) using MinKNOW version 25.05.14 and Dorado version 7.9.8.
1137

1138 **Nanopore Sequencing Analysis of mRNA Poly(A) Tails and Abundance**

1139 Nanopore pod5 files were simultaneously basecalled and aligned to the hg38[128] human reference genome
1140 using the Dorado basecaller (v0.9.0; https://github.com/nanoporetech/dorado). Poly(A) tail measurements
1141 for each read were also called with Dorado (full command: dorado basecaller hac "$pod5_files" --device
1142 cuda:0 --estimate-poly-a --reference "$reference" --mm2-opts "-k 15 -w 10" --min-qscore 9 > "$output_file").
1143 Non-primary alignments were filtered out using samtools[129] (v1.21). Reads were then assigned to genetic
1144 features using featureCounts[130] (v2.1.1) and the NCBI Refseq hg38 gtf annotation file[128]. Poly(A) tail lengths
1145 were averaged across reads for each gene. Genes for which there were fewer than 10 reads were excluded
1146 from the analysis. Only reads mapping to the nuclear genome were included. Classifications for RNAs
1147 enriched in stress granules were taken from Khong et al., 2017[30].
1148 Differential expression analysis was conducted using DESeq2[103]. Input count tables were generated from
1149 featureCounts[129]. Scripts for this analysis can be accessed on Github
1150 (https://github.com/wormbro1/Tsai_et_al_CCR4NOT_DRS_analysis). Poly(A) length analysis was
1151 conducted using TAILCaller[101] to identify significant changes with p_{adj} <0.05 and >|1.3|-fold in median
1152 lengths. Subsequent post-hoc condition-condition comparisons were completed based on initial test
1153 determined by TAILCaller; Dunn's test for Kruskal-Wallis, Tukey's HSD test for ANOVA, and Games-Howell
1154 test for Welch's ANOVA. All post-hoc tests were corrected with Bonferroni adjustment, save for Games-

1155 Howell, which has adjustments built-in. Fold-change of poly(A) lengths was calculated from the median
1156 poly(A) length for each gene, as calculated by TAILCaller.
1157
1158 **RT-qPCR**
1159 100ng to 1 µg of RNA was used to prepare cDNA using qSCRIPT cDNA Synthesis Kit (QuantaBio, #95047-
1160 100) following the manufacturer's protocol. Prior to reverse transcription, 25ng of *Saccharomyces*
1161 *cerevisiae* RNA for ENO2 was spiked into the RNA samples used as an internal control. RT-qPCR master
1162 mixes were prepared using the appropriate forward and reverse primers (Table S10) and PerfeCTa SYBR
1163 Green FastMix (QuantaBio, #95072-012). The qPCR was completed using a Bio-Rad CFX Connect. For
1164 all RT-qPCR experiments, 18S rRNA was used as an internal control to normalize Cq values.
1165
1166 **DATA AVAILABILITY**
1167 All proteomics data are available at the Mass Spectrometry Interactive Virtual Environment (MassIVE,
1168 http://massive.ucsd.edu). MassIVE ID: MSV000095953 (ftp://massive.ucsd.edu/v08/MSV000095953/);
1169 MassIVE ID: MSV000095944 (ftp://massive.ucsd.edu/v08/MSV000095944/); MassIVE ID: MSV000098662
1170 (ftp://massive-ftp.ucsd.edu/v10/MSV000098662/); and MassIVE ID: MSV000100193 (ftp://massive-
1171 ftp.ucsd.edu/v11/MSV000100193/).
1172
1173 Nanopore data are available at the European Nucleotide Archive. Nanopore ENA accession number:
1174 PRJEB106356 (https://www.ebi.ac.uk/ena/browser/view/PRJEB106356).
1175
1176 **CODE AVAILABILITY**
1177 Data analysis and visualization codes will be shared upon request to the lead contact, Ji-Young Youn
1178 (jiyoung.youn@sickkids.ca).
1179
1180

1181 **REFERENCES**

1182 1 Cheng, Z. *et al.* Differential dynamics of the mammalian mRNA and protein
1183 expression response to misfolding stress. *Mol Syst Biol* **12**, 855 (2016).
1184 https://doi.org:10.15252/msb.20156423
1185 2 Gomez-Pastor, R., Burchfiel, E. T. & Thiele, D. J. Regulation of heat shock
1186 transcription factors and their roles in physiology and disease. *Nat Rev Mol Cell*
1187 *Biol* **19**, 4-19 (2018). https://doi.org:10.1038/nrm.2017.73
1188 3 Christopher, J. A. *et al.* Subcellular proteomics. *Nat Rev Methods Primers* **1**
1189 (2021). https://doi.org:10.1038/s43586-021-00029-y
1190 4 Lundberg, E. & Borner, G. H. H. Spatial proteomics: a powerful discovery tool for
1191 cell biology. *Nat Rev Mol Cell Biol* **20**, 285-302 (2019).
1192 https://doi.org:10.1038/s41580-018-0094-y
1193 5 Villanueva, E. *et al.* System-wide analysis of RNA and protein subcellular
1194 localization dynamics. *Nat Methods* **21**, 60-71 (2024).
1195 https://doi.org:10.1038/s41592-023-02101-9
1196 6 Chong, Y. T. *et al.* Yeast Proteome Dynamics from Single Cell Imaging and
1197 Automated Analysis. *Cell* **161**, 1413-1424 (2015).
1198 https://doi.org:10.1016/j.cell.2015.04.051
1199 7 Christoforou, A. *et al.* A draft map of the mouse pluripotent stem cell spatial
1200 proteome. *Nat Commun* **7**, 8992 (2016). https://doi.org:10.1038/ncomms9992
1201 8 Dionne, U. & Gingras, A. C. Proximity-Dependent Biotinylation Approaches to
1202 Explore the Dynamic Compartmentalized Proteome. *Front Mol Biosci* **9**, 852911
1203 (2022). https://doi.org:10.3389/fmolb.2022.852911
1204 9 Go, C. D. *et al.* A Proximity-Dependent Biotinylation Map of a Human Cell. *Nature*
1205 **595**, 120-124 (2021). https://doi.org:10.1038/s41586-021-03592-2
1206 10 Huh, W. K. *et al.* Global analysis of protein localization in budding yeast. *Nature*
1207 **425**, 686-691 (2003). https://doi.org:10.1038/nature02026
1208 11 Itzhak, D. N., Tyanova, S., Cox, J. & Borner, G. H. Global, quantitative and dynamic
1209 mapping of protein subcellular localization. *Elife* **5** (2016).
1210 https://doi.org:10.7554/eLife.16950
1211 12 Thul, P. J. *et al.* A subcellular map of the human proteome. *Science* **356** (2017).
1212 https://doi.org:10.1126/science.aal3321
1213 13 Breker, M., Gymrek, M. & Schuldiner, M. A novel single-cell screening platform
1214 reveals proteome plasticity during yeast stress responses. *J Cell Biol* **200**, 839-
1215 850 (2013). https://doi.org:10.1083/jcb.201301120
1216 14 Jean Beltran, P. M., Mathias, R. A. & Cristea, I. M. A Portrait of the Human
1217 Organelle Proteome In Space and Time during Cytomegalovirus Infection. *Cell*
1218 *Syst* **3**, 361-373 e366 (2016). https://doi.org:10.1016/j.cels.2016.08.012
1219 15 Lu, A. X. *et al.* Integrating images from multiple microscopy screens reveals
1220 diverse patterns of change in the subcellular localization of proteins. *Elife* **7** (2018).
1221 https://doi.org:10.7554/eLife.31872
1222 16 Tkach, J. M. *et al.* Dissecting DNA damage response pathways by analysing
1223 protein localization and abundance changes during DNA replication stress. *Nat*
1224 *Cell Biol* **14**, 966-976 (2012). https://doi.org:10.1038/ncb2549

1225 17 Alberti, S. & Hyman, A. A. Biomolecular condensates at the nexus of cellular
1226 stress, protein aggregation disease and ageing. *Nat Rev Mol Cell Biol* **22**, 196-213
1227 (2021). https://doi.org:10.1038/s41580-020-00326-6
1228 18 Rabouille, C. & Alberti, S. Cell adaptation upon stress: the emerging role of
1229 membrane-less compartments. *Curr Opin Cell Biol* **47**, 34-42 (2017).
1230 https://doi.org:10.1016/j.ceb.2017.02.006
1231 19 Banani, S. F., Lee, H. O., Hyman, A. A. & Rosen, M. K. Biomolecular Condensates:
1232 Organizers of Cellular Biochemistry. *Nat Rev Mol Cell Biol* **18**, 285-298 (2017).
1233 https://doi.org:10.1038/nrm.2017.7
1234 20 Shin, Y. & Brangwynne, C. P. Liquid phase condensation in cell physiology and
1235 disease. *Science* **357** (2017). https://doi.org:10.1126/science.aaf4382
1236 21 Case, L. B., Zhang, X., Ditlev, J. A. & Rosen, M. K. Stoichiometry controls activity
1237 of phase-separated clusters of actin signaling proteins. *Science* **363**, 1093-1097
1238 (2019). https://doi.org:10.1126/science.aau6313
1239 22 Franzmann, T. M. *et al.* Phase separation of a yeast prion protein promotes cellular
1240 fitness. *Science* **359** (2018). https://doi.org:10.1126/science.aao5654
1241 23 Klosin, A. *et al.* Phase separation provides a mechanism to reduce noise in cells.
1242 *Science* **367**, 464-468 (2020). https://doi.org:10.1126/science.aav6691
1243 24 Riback, J. A. *et al.* Stress-Triggered Phase Separation Is an Adaptive,
1244 Evolutionarily Tuned Response. *Cell* **168**, 1028-1040 e1019 (2017).
1245 https://doi.org:10.1016/j.cell.2017.02.027
1246 25 Shin, Y. *et al.* Liquid Nuclear Condensates Mechanically Sense and Restructure
1247 the Genome. *Cell* **175**, 1481-1491 e1413 (2018).
1248 https://doi.org:10.1016/j.cell.2018.10.057
1249 26 Costa-Mattioli, M. & Walter, P. The integrated stress response: From mechanism
1250 to disease. *Science* **368** (2020). https://doi.org:10.1126/science.aat5314
1251 27 McCormick, C. & Khaperskyy, D. A. Translation Inhibition and Stress Granules in
1252 the Antiviral Immune Response. *Nat Rev Immunol* **17**, 647-660 (2017).
1253 https://doi.org:10.1038/nri.2017.63
1254 28 Hofmann, S., Kedersha, N., Anderson, P. & Ivanov, P. Molecular Mechanisms of
1255 Stress Granule Assembly and Disassembly. *Biochim Biophys Acta Mol Cell Res*
1256 **1868**, 118876 (2021). https://doi.org:10.1016/j.bbamcr.2020.118876
1257 29 Ivanov, P., Kedersha, N. & Anderson, P. Stress Granules and Processing Bodies
1258 in Translational Control. *Cold Spring Harb Perspect Biol* **11** (2019).
1259 https://doi.org:10.1101/cshperspect.a032813
1260 30 Khong, A. *et al.* The Stress Granule Transcriptome Reveals Principles of mRNA
1261 Accumulation in Stress Granules. *Mol Cell* **68**, 808-820 (2017).
1262 https://doi.org:10.1016/j.molcel.2017.10.015
1263 31 Millar, S. R. *et al.* A New Phase of Networking: The Molecular Composition and
1264 Regulatory Dynamics of Mammalian Stress Granules. *Chem Rev* **123**, 9036-9064
1265 (2023). https://doi.org:10.1021/acs.chemrev.2c00608
1266 32 Kedersha, N., Ivanov, P. & Anderson, P. Stress granules and cell signaling: more
1267 than just a passing phase? *Trends Biochem Sci* **38**, 494-506 (2013).
1268 https://doi.org:10.1016/j.tibs.2013.07.004

1269 33 Panas, M. D., Ivanov, P. & Anderson, P. Mechanistic insights into mammalian
1270 stress granule dynamics. *J Cell Biol* **215**, 313-323 (2016).
1271 https://doi.org:10.1083/jcb.201609081
1272 34 Arimoto, K., Fukuda, H., Imajoh-Ohmi, S., Saito, H. & Takekawa, M. Formation of
1273 Stress Granules Inhibits Apoptosis by Suppressing Stress-Responsive MAPK
1274 Pathways. *Nat Cell Biol* **10**, 1324-1332 (2008). https://doi.org:10.1038/ncb1791
1275 35 Samir, P. *et al.* DDX3X Acts as a Live-or-Die Checkpoint in Stressed Cells by
1276 Regulating NLRP3 Inflammasome. *Nature* **573**, 590-594 (2019).
1277 https://doi.org:10.1038/s41586-019-1551-2
1278 36 Thedieck, K. *et al.* Inhibition of mTORC1 by astrin and stress granules prevents
1279 apoptosis in cancer cells. *Cell* **154**, 859-874 (2013).
1280 https://doi.org:10.1016/j.cell.2013.07.031
1281 37 Markmiller, S. *et al.* Context-Dependent and Disease-Specific Diversity in Protein
1282 Interactions within Stress Granules. *Cell* **172**, 590-604 (2018).
1283 https://doi.org:10.1016/j.cell.2017.12.032
1284 38 Fujimura, K., Sasaki, A. T. & Anderson, P. Selenite targets eIF4E-binding protein-
1285 1 to inhibit translation initiation and induce the assembly of non-canonical stress
1286 granules. *Nucleic Acids Res* **40**, 8099-8110 (2012).
1287 https://doi.org:10.1093/nar/gks566
1288 39 Hernandez-Elvira, M. & Sunnerhagen, P. Post-transcriptional regulation during
1289 stress. *FEMS Yeast Res* **22** (2022). https://doi.org:10.1093/femsyr/foac025
1290 40 Morano, K. A., Grant, C. M. & Moye-Rowley, W. S. The response to heat shock
1291 and oxidative stress in Saccharomyces cerevisiae. *Genetics* **190**, 1157-1195
1292 (2012). https://doi.org:10.1534/genetics.111.128033
1293 41 Rosa-Mercado, N. A. *et al.* Hyperosmotic stress alters the RNA polymerase II
1294 interactome and induces readthrough transcription despite widespread
1295 transcriptional repression. *Mol Cell* **81**, 502-513 e504 (2021).
1296 https://doi.org:10.1016/j.molcel.2020.12.002
1297 42 Vihervaara, A., Duarte, F. M. & Lis, J. T. Molecular mechanisms driving
1298 transcriptional stress responses. *Nat Rev Genet* **19**, 385-397 (2018).
1299 https://doi.org:10.1038/s41576-018-0001-6
1300 43 Voth, W. & Jakob, U. Stress-Activated Chaperones: A First Line of Defense.
1301 *Trends Biochem Sci* **42**, 899-913 (2017). https://doi.org:10.1016/j.tibs.2017.08.006
1302 44 Passmore, L. A. & Coller, J. Roles of mRNA poly(A) tails in regulation of eukaryotic
1303 gene expression. *Nat Rev Mol Cell Biol* **23**, 93-106 (2022).
1304 https://doi.org:10.1038/s41580-021-00417-y
1305 45 Yi, H. *et al.* PABP Cooperates with the CCR4-NOT Complex to Promote mRNA
1306 Deadenylation and Block Precocious Decay. *Mol Cell* **70**, 1081-1088 e1085
1307 (2018). https://doi.org:10.1016/j.molcel.2018.05.009
1308 46 Bianchin, C., Mauxion, F., Sentis, S., Seraphin, B. & Corbo, L. Conservation of the
1309 deadenylase activity of proteins of the Caf1 family in human. *RNA* **11**, 487-494
1310 (2005). https://doi.org:10.1261/rna.7135305
1311 47 Yamashita, A. *et al.* Concerted action of poly(A) nucleases and decapping enzyme
1312 in mammalian mRNA turnover. *Nat Struct Mol Biol* **12**, 1054-1063 (2005).
1313 https://doi.org:10.1038/nsmb1016

1314 48 Braun, J. E., Huntzinger, E., Fauser, M. & Izaurralde, E. GW182 proteins directly
1315 recruit cytoplasmic deadenylase complexes to miRNA targets. *Mol Cell* **44**, 120-
1316 133 (2011). https://doi.org:10.1016/j.molcel.2011.09.007
1317 49 Collart, M. A. & Timmers, H. T. The eukaryotic Ccr4-not complex: a regulatory
1318 platform integrating mRNA metabolism with cellular signaling pathways? *Prog*
1319 *Nucleic Acid Res Mol Biol* **77**, 289-322 (2004). https://doi.org:10.1016/S0079-
1320 6603(04)77008-7
1321 50 Fabian, M. R. *et al.* miRNA-mediated deadenylation is orchestrated by GW182
1322 through two conserved motifs that interact with CCR4-NOT. *Nat Struct Mol Biol* **18**,
1323 1211-1217 (2011). https://doi.org:10.1038/nsmb.2149
1324 51 Flavell, A. Introns continue to amaze. *Nature* **316**, 574-575 (1985).
1325 https://doi.org:10.1038/316574a0
1326 52 Huntzinger, E. *et al.* The interactions of GW182 proteins with PABP and
1327 deadenylases are required for both translational repression and degradation of
1328 miRNA targets. *Nucleic Acids Res* **41**, 978-994 (2013).
1329 https://doi.org:10.1093/nar/gks1078
1330 53 Ito, K. *et al.* CNOT2 depletion disrupts and inhibits the CCR4-NOT deadenylase
1331 complex and induces apoptotic cell death. *Genes Cells* **16**, 368-379 (2011).
1332 https://doi.org:10.1111/j.1365-2443.2011.01492.x
1333 54 Raisch, T. *et al.* Distinct modes of recruitment of the CCR4-NOT complex by
1334 Drosophila and vertebrate Nanos. *EMBO J* **35**, 974-990 (2016).
1335 https://doi.org:10.15252/embj.201593634
1336 55 Russell, P., Benson, J. D. & Denis, C. L. Characterization of mutations in NOT2
1337 indicates that it plays an important role in maintaining the integrity of the CCR4-
1338 NOT complex. *J Mol Biol* **322**, 27-39 (2002). https://doi.org:10.1016/s0022-
1339 2836(02)00707-6
1340 56 Tudek, A. *et al.* Global view on the metabolism of RNA poly(A) tails in yeast
1341 Saccharomyces cerevisiae. *Nat Commun* **12**, 4951 (2021).
1342 https://doi.org:10.1038/s41467-021-25251-w
1343 57 Woo, Y. M. *et al.* TED-Seq Identifies the Dynamics of Poly(A) Length during ER
1344 Stress. *Cell Rep* **24**, 3630-3641 e3637 (2018).
1345 https://doi.org:10.1016/j.celrep.2018.08.084
1346 58 Yamagishi, R., Hosoda, N. & Hoshino, S. Arsenite inhibits mRNA deadenylation
1347 through proteolytic degradation of Tob and Pan3. *Biochem Biophys Res Commun*
1348 **455**, 323-331 (2014). https://doi.org:10.1016/j.bbrc.2014.11.015
1349 59 Dar, S. A. *et al.* Full-length direct RNA sequencing uncovers stress granule-
1350 dependent RNA decay upon cellular stress. *Elife* **13** (2024).
1351 https://doi.org:10.7554/eLife.96284
1352 60 Hilgers, V., Teixeira, D. & Parker, R. Translation-independent inhibition of mRNA
1353 deadenylation during stress in Saccharomyces cerevisiae. *RNA* **12**, 1835-1845
1354 (2006). https://doi.org:10.1261/rna.241006
1355 61 Yamagishi, R. *et al.* Concerted action of ataxin-2 and PABPC1-bound mRNA
1356 poly(A) tail in the formation of stress granules. *Nucleic Acids Res* **52**, 9193-9209
1357 (2024). https://doi.org:10.1093/nar/gkae497
1358 62 Marmor-Kollet, H. *et al.* Spatiotemporal Proteomic Analysis of Stress Granule
1359 Disassembly Using APEX Reveals Regulation by SUMOylation and Links to ALS

Pathogenesis. *Mol Cell* **80**, 876-891 (2020). https://doi.org:10.1016/j.molcel.2020.10.032

63 Youn, J. Y. *et al.* High-Density Proximity Mapping Reveals the Subcellular Organization of mRNA-Associated Granules and Bodies. *Mol Cell* **69**, 517-532 (2018). https://doi.org:10.1016/j.molcel.2017.12.020

64 Branon, T. C. *et al.* Efficient Proximity Labeling in Living Cells and Organisms with TurboID. *Nat Biotechnol* **36**, 880-887 (2018). https://doi.org:10.1038/nbt.4201

65 Choi, H. *et al.* SAINT: probabilistic scoring of affinity purification-mass spectrometry data. *Nat Methods* **8**, 70-73 (2011). https://doi.org:10.1038/nmeth.1541

66 Teo, G. *et al.* SAINTexpress: improvements and additional features in Significance Analysis of INTeractome software. *J Proteomics* **100**, 37-43 (2014). https://doi.org:10.1016/j.jprot.2013.10.023

67 Uechi, H. *et al.* Small-molecule dissolution of stress granules by redox modulation benefits ALS models. *Nat Chem Biol* (2025). https://doi.org:10.1038/s41589-025-01893-5

68 Aulas, A. *et al.* Stress-Specific Differences in Assembly and Composition of Stress Granules and Related Foci. *J Cell Sci* **130**, 927-937 (2017). https://doi.org:10.1242/jcs.199240

69 Kedersha, N. *et al.* G3BP-Caprin1-USP10 complexes mediate stress granule condensation and associate with 40S subunits. *J Cell Biol* **212**, 845-860 (2016). https://doi.org:10.1083/jcb.201508028

70 Bounedjah, O. *et al.* Macromolecular crowding regulates assembly of mRNA stress granules after osmotic stress: new role for compatible osmolytes. *J Biol Chem* **287**, 2446-2458 (2012). https://doi.org:10.1074/jbc.M111.292748

71 Romero-Perez, P. S., Dorone, Y., Flores, E., Sukenik, S. & Boeynaems, S. When Phased without Water: Biophysics of Cellular Desiccation, from Biomolecules to Condensates. *Chem Rev* **123**, 9010-9035 (2023). https://doi.org:10.1021/acs.chemrev.2c00659

72 Shu, T. *et al.* Mesoscale molecular assembly is favored by the active, crowded cytoplasm. *bioRxiv* (2023). https://doi.org:10.1101/2023.09.19.558334

73 Barzilai, A. & Yamamoto, K. DNA damage responses to oxidative stress. *DNA Repair (Amst)* **3**, 1109-1115 (2004). https://doi.org:10.1016/j.dnarep.2004.03.002

74 Kehm, R., Baldensperger, T., Raupbach, J. & Hohn, A. Protein oxidation - Formation mechanisms, detection and relevance as biomarkers in human diseases. *Redox Biol* **42**, 101901 (2021). https://doi.org:10.1016/j.redox.2021.101901

75 Korotkov, S. M. Mitochondrial Oxidative Stress Is the General Reason for Apoptosis Induced by Different-Valence Heavy Metals in Cells and Mitochondria. *Int J Mol Sci* **24** (2023). https://doi.org:10.3390/ijms241914459

76 Boyd-Shiwarski, C. R. *et al.* WNK kinases sense molecular crowding and rescue cell volume via phase separation. *Cell* **185**, 4488-4506 e4420 (2022). https://doi.org:10.1016/j.cell.2022.09.042

77 Xiao, Y. X. *et al.* The TSC22D, WNK, and NRBP gene families exhibit functional buffering and evolved with Metazoa for cell volume regulation. *Cell Rep* **43**, 114417 (2024). https://doi.org:10.1016/j.celrep.2024.114417

78 Guillen-Boixet, J. *et al.* RNA-Induced Conformational Switching and Clustering of G3BP Drive Stress Granule Assembly by Condensation. *Cell* **181**, 346-361 (2020). https://doi.org:10.1016/j.cell.2020.03.049

79 Ivanov, P. A., Chudinova, E. M. & Nadezhdina, E. S. Disruption of microtubules inhibits cytoplasmic ribonucleoprotein stress granule formation. *Exp Cell Res* **290**, 227-233 (2003). https://doi.org:10.1016/s0014-4827(03)00290-8

80 Loschi, M., Leishman, C. C., Berardone, N. & Boccaccio, G. L. Dynein and kinesin regulate stress-granule and P-body dynamics. *J Cell Sci* **122**, 3973-3982 (2009). https://doi.org:10.1242/jcs.051383

81 Demichev, V., Messner, C. B., Vernardis, S. I., Lilley, K. S. & Ralser, M. DIA-NN: neural networks and interference correction enable deep proteome coverage in high throughput. *Nat Methods* **17**, 41-44 (2020). https://doi.org:10.1038/s41592-019-0638-x

82 Teo, G. *et al.* SAINTq: Scoring protein-protein interactions in affinity purification - mass spectrometry experiments with fragment or peptide intensity data. *Proteomics* **16**, 2238-2245 (2016). https://doi.org:10.1002/pmic.201500499

83 Hutten, S. & Dormann, D. A Quantitative Assay to Measure Stress Granule Association of Proteins and Peptidesin Semi-permeabilized Human Cells. *Bio Protoc* **10**, e3846 (2020). https://doi.org:10.21769/BioProtoc.3846

84 Wu, Y. *et al.* Translation landscape of stress granules. *Sci Adv* **11**, eady6859 (2025). https://doi.org:10.1126/sciadv.ady6859

85 Lu, H. *et al.* Chemotherapy triggers HIF-1-dependent glutathione synthesis and copper chelation that induces the breast cancer stem cell phenotype. *Proc Natl Acad Sci U S A* **112**, E4600-4609 (2015). https://doi.org:10.1073/pnas.1513433112

86 Turakhiya, A. *et al.* ZFAND1 Recruits p97 and the 26S Proteasome to Promote the Clearance of Arsenite-Induced Stress Granules. *Mol Cell* **70**, 906-919 e907 (2018). https://doi.org:10.1016/j.molcel.2018.04.021

87 Boeynaems, S. *et al.* Spontaneous driving forces give rise to protein-RNA condensates with coexisting phases and complex material properties. *Proc Natl Acad Sci U S A* **116**, 7889-7898 (2019). https://doi.org:10.1073/pnas.1821038116

88 Eisenberg, H. & Felsenfeld, G. Studies of the temperature-dependent conformation and phase separation of polyriboadenylic acid solutions at neutral pH. *J Mol Biol* **30**, 17-37 (1967). https://doi.org:10.1016/0022-2836(67)90240-9

89 Jain, A. & Vale, R. D. RNA phase transitions in repeat expansion disorders. *Nature* **546**, 243-247 (2017). https://doi.org:10.1038/nature22386

90 Van Treeck, B. *et al.* RNA Self-Assembly Contributes to Stress Granule Formation and Defining the Stress Granule Transcriptome. *Proc Natl Acad Sci U S A* **115**, 2734-2739 (2018). https://doi.org:10.1073/pnas.1800038115

91 Wadsworth, G. M. *et al.* RNAs undergo phase transitions with lower critical solution temperatures. *Nat Chem* **15**, 1693-1704 (2023). https://doi.org:10.1038/s41557-023-01353-4

92 Kondrashov, A. *et al.* Inhibition of polyadenylation reduces inflammatory gene induction. *RNA* **18**, 2236-2250 (2012). https://doi.org:10.1261/rna.032391.112

1450 93 Burgess, H. M. *et al.* CCR4-NOT differentially controls host versus virus poly(a)-
1451 tail length and regulates HCMV infection. *EMBO Rep* **24**, e56327 (2023).
1452 https://doi.org:10.15252/embr.202256327
1453 94 Suzuki, T. *et al.* Regulation of CCR4-NOT complex deadenylase activity and
1454 cellular responses by MK2-dependent phosphorylation of CNOT2. *RNA Biol* **19**,
1455 234-246 (2022). https://doi.org:10.1080/15476286.2021.2021676
1456 95 Cougot, N., Babajko, S. & Seraphin, B. Cytoplasmic foci are sites of mRNA decay
1457 in human cells. *J Cell Biol* **165**, 31-40 (2004).
1458 https://doi.org:10.1083/jcb.200309008
1459 96 Zheng, D. *et al.* Deadenylation is prerequisite for P-body formation and mRNA
1460 decay in mammalian cells. *J Cell Biol* **182**, 89-101 (2008).
1461 https://doi.org:10.1083/jcb.200801196
1462 97 Kedersha, N. *et al.* Stress granules and processing bodies are dynamically linked
1463 sites of mRNP remodeling. *J Cell Biol* **169**, 871-884 (2005).
1464 https://doi.org:10.1083/jcb.200502088
1465 98 Panasenko, O. O. *et al.* Co-translational assembly of proteasome subunits in
1466 NOT1-containing assemblysomes. *Nat Struct Mol Biol* **26**, 110-120 (2019).
1467 https://doi.org:10.1038/s41594-018-0179-5
1468 99 Gombas, B. G., Nemeth-Szatmari, O., Nagy-Miko, B. & Villanyi, Z. Role of
1469 Assemblysomes in Cellular Stress Responses. *Wiley Interdiscip Rev RNA* **16**,
1470 e70009 (2025). https://doi.org:10.1002/wrna.70009
1471 100 Raisch, T. & Valkov, E. Regulation of the multisubunit CCR4-NOT deadenylase in
1472 the initiation of mRNA degradation. *Curr Opin Struct Biol* **77**, 102460 (2022).
1473 https://doi.org:10.1016/j.sbi.2022.102460
1474 101 Mazdziarz, M., Paukszto, L. & Sawicki, J. TAILcaller: an R package for analyzing
1475 differences in poly(A) tail length for Oxford Nanopore RNA sequencing. *Bioinform*
1476 *Adv* **5**, vbaf235 (2025). https://doi.org:10.1093/bioadv/vbaf235
1477 102 Love, M. I., Huber, W. & Anders, S. Moderated estimation of fold change and
1478 dispersion for RNA-seq data with DESeq2. *Genome Biol* **15**, 550 (2014).
1479 https://doi.org:10.1186/s13059-014-0550-8
1480 103 Pakos-Zebrucka, K. *et al.* The integrated stress response. *EMBO Rep* **17**, 1374-
1481 1395 (2016). https://doi.org:10.15252/embr.201642195
1482 104 Lavoie, H., Gagnon, J. & Therrien, M. ERK signalling: a master regulator of cell
1483 behaviour, life and fate. *Nat Rev Mol Cell Biol* **21**, 607-632 (2020).
1484 https://doi.org:10.1038/s41580-020-0255-7
1485 105 Jain, S. *et al.* ATPase-Modulated Stress Granules Contain a Diverse Proteome
1486 and Substructure. *Cell* **164**, 487-498 (2016).
1487 https://doi.org:10.1016/j.cell.2015.12.038
1488 106 Costanzo, M. *et al.* A global genetic interaction network maps a wiring diagram of
1489 cellular function. *Science* **353** (2016). https://doi.org:10.1126/science.aaf1420
1490 107 VanderSluis, B. *et al.* Integrating genetic and protein-protein interaction networks
1491 maps a functional wiring diagram of a cell. *Curr. Opin. Microbiol.* **45**, 170-179
1492 (2018). https://doi.org:10.1016/j.mib.2018.06.004
1493 108 Matheny, T., Van Treeck, B., Huynh, T. N. & Parker, R. RNA Partitioning into
1494 Stress Granules is Based on the Summation of Multiple Interactions. *RNA* **27**, 174-
1495 189 (2021). https://doi.org:10.1261/rna.078204.120

109 Huang, J. Q. *et al.* PRRC2A, PRRC2B and PRRC2C are Stress Granule Proteins that Promote Translation Through Association with the eIF3 complex. *bioRxiv*, 2026.2002.2024.707808 (2026). https://doi.org:10.64898/2026.02.24.707808

110 Astrom, J., Astrom, A. & Virtanen, A. In vitro deadenylation of mammalian mRNA by a HeLa cell 3' exonuclease. *EMBO J* **10**, 3067-3071 (1991). https://doi.org:10.1002/j.1460-2075.1991.tb07858.x

111 Schreiber, K. J., Kadijk, E. & Youn, J. Y. Exploring Options for Proximity-Dependent Biotinylation Experiments: Comparative Analysis of Labeling Enzymes and Affinity Purification Resins. *J Proteome Res* **23**, 1531-1543 (2024). https://doi.org:10.1021/acs.jproteome.3c00908

112 Esmaeili Anvar, N. *et al.* Efficient gene knockout and genetic interaction screening using the in4mer CRISPR/Cas12a multiplex knockout platform. *Nat Commun* **15**, 3577 (2024). https://doi.org:10.1038/s41467-024-47795-3

113 Gibson, D. G. *et al.* Enzymatic assembly of DNA molecules up to several hundred kilobases. *Nat Methods* **6**, 343-345 (2009). https://doi.org:10.1038/nmeth.1318

114 Poser, I. *et al.* BAC TransgeneOmics: a high-throughput method for exploration of protein function in mammals. *Nat Methods* **5**, 409-415 (2008). https://doi.org:10.1038/nmeth.1199

115 Schmidt, E. K., Clavarino, G., Ceppi, M. & Pierre, P. SUnSET, a nonradioactive method to monitor protein synthesis. *Nat Methods* **6**, 275-277 (2009). https://doi.org:10.1038/nmeth.1314

116 Youn, J. Y. *et al.* Properties of Stress Granule and P-Body Proteomes. *Mol Cell* **76**, 286-294 (2019). https://doi.org:10.1016/j.molcel.2019.09.014

117 Pino, L. K., Just, S. C., MacCoss, M. J. & Searle, B. C. Acquiring and Analyzing Data Independent Acquisition Proteomics Experiments without Spectrum Libraries. *Mol Cell Proteomics* **19**, 1088-1103 (2020). https://doi.org:10.1074/mcp.P119.001913

118 Kong, A. T., Leprevost, F. V., Avtonomov, D. M., Mellacheruvu, D. & Nesvizhskii, A. I. MSFragger: ultrafast and comprehensive peptide identification in mass spectrometry-based proteomics. *Nat Methods* **14**, 513-520 (2017). https://doi.org:10.1038/nmeth.4256

119 Yu, F., Haynes, S. E. & Nesvizhskii, A. I. IonQuant Enables Accurate and Sensitive Label-Free Quantification With FDR-Controlled Match-Between-Runs. *Mol Cell Proteomics* **20**, 100077 (2021). https://doi.org:10.1016/j.mcpro.2021.100077

120 da Veiga Leprevost, F. *et al.* Philosopher: a versatile toolkit for shotgun proteomics data analysis. *Nat Methods* **17**, 869-870 (2020). https://doi.org:10.1038/s41592-020-0912-y

121 Yang, K. L. *et al.* MSBooster: improving peptide identification rates using deep learning-based features. *Nat Commun* **14**, 4539 (2023). https://doi.org:10.1038/s41467-023-40129-9

122 The, M., MacCoss, M. J., Noble, W. S. & Kall, L. Fast and Accurate Protein False Discovery Rates on Large-Scale Proteomics Data Sets with Percolator 3.0. *J Am Soc Mass Spectrom* **27**, 1719-1727 (2016). https://doi.org:10.1007/s13361-016-1460-7

123 Nesvizhskii, A. I., Keller, A., Kolker, E. & Aebersold, R. A statistical model for identifying proteins by tandem mass spectrometry. *Anal Chem* **75**, 4646-4658 (2003). https://doi.org:10.1021/ac0341261

124 Yu, F. *et al.* Fast Quantitative Analysis of timsTOF PASEF Data with MSFragger and IonQuant. *Mol Cell Proteomics* **19**, 1575-1585 (2020). https://doi.org:10.1074/mcp.TIR120.002048

125 Schubert, O. T. *et al.* Building high-quality assay libraries for targeted analysis of SWATH MS data. *Nat Protoc* **10**, 426-441 (2015). https://doi.org:10.1038/nprot.2015.015

126 Choi, H. *et al.* Analyzing protein-protein interactions from affinity purification-mass spectrometry data with SAINT. *Curr Protoc Bioinformatics* **Chapter 8**, 8 15 11-18 15 23 (2012). https://doi.org:10.1002/0471250953.bi0815s39

127 McQuin, C. *et al.* CellProfiler 3.0: Next-generation image processing for biology. *PLoS Biol.* **16**, e2005970 (2018). https://doi.org:10.1371/journal.pbio.2005970

128 Perez, G. *et al.* The UCSC Genome Browser database: 2025 update. *Nucleic Acids Res.* **53**, D1243-D1249 (2025). https://doi.org:10.1093/nar/gkae974

129 Li, H. *et al.* The Sequence Alignment/Map format and SAMtools. *Bioinformatics* **25**, 2078-2079 (2009). https://doi.org:10.1093/bioinformatics/btp352

130 Liao, Y., Smyth, G. K. & Shi, W. featureCounts: an efficient general purpose program for assigning sequence reads to genomic features. *Bioinformatics* **30**, 923-930 (2014). https://doi.org:10.1093/bioinformatics/btt656

131 Knight, J. D. R. *et al.* ProHits-viz: a suite of web tools for visualizing interaction proteomics data. *Nat Methods* **14**, 645-646 (2017). https://doi.org:10.1038/nmeth.4330

1567 **ACKNOWLEDGEMENT**

1568 We thank A.C. Gingras for supervising V. Kasmaeifar; B. Larsen, C. Wong, G. Liu, and H.W. Choi for help
1569 with proteomics and SAINTq analysis; D. Haakonsen for the technical guide for using the Cas12a system;
1570 K. Talipova and L. Pelletier for their contribution to validation. We thank Tara Paton and Sachin at TCAG
1571 for their Nanopore DRS processing and thank J.L. Rubinstein for his review of the manuscript. This work
1572 was supported by the Natural Sciences and Engineering Research Council of Canada (NSERC; RGPIN-
1573 2022-04849), Canada Foundation for Innovation (CFI; 41430) and the Canadian Institutes of Health
1574 Research (481147) to J.-Y.Y, National Institutes of Health (R35GM128680) to O.R. Confocal imaging was
1575 performed at the SickKids Imaging Facility, a facility supported by Canada Foundation for Innovation,
1576 Ontario Research Fund and SickKids Research Institute. H.R. is the Canada Research Chair (Tier 2) in
1577 Mass Spectrometry-based Personalized Medicine and J.-Y.Y is the Canada Research Chair (Tier 2) in
1578 Membraneless Organelle Proteomics.

1579

1580 **AUTHOR CONTRIBUTIONS**

1581 Conceptualization, J.-Y.Y., A. H.; Methodology, Y.-C.T., H.U., S.R.M., E.K., K.J.S., R.B., C.M., A.J.;
1582 Software, Y.-C.T., V.K.; Validation, E.K., A.M.; Formal Analysis, Y.-C.T., H.U., S.R.M., K.J.S., J.P.T.O.,
1583 J.Q.H.; Investigation, Y.-C.T., H.U., S.R.M., E.K., K.J.S., A.M., Z.Z., J.S.; Resources, C.A.L., J.Q.H.; Data
1584 Curation, Y.-C.T.; Writing – Original Draft, J.-Y.Y., H.U., Y.-C.T.; Writing – Review & Editing, H.U., Y.-C.T.,
1585 E.K., A.M., K.J.S., J.Q.H., H.R., A.H., J.-Y.Y.; Visualization, Y.-C.T., H.U., J.-Y.Y.; Supervision, J.-Y.Y., A.
1586 H. H.R., O.S.R.; Project Administration, J.-Y.Y. H.R., H.U., A. H.; and Funding Acquisition, J.-Y.Y., H.R., A.
1587 H.

1588

1589 **DECLARATION OF INTERESTS**

1590 A.A.H. is a founder and scientific adviser board member of Dewpoint Therapeutics.

1591

1592 **DECLARATION OF GENERATIVE AI AND AI-ASSISTED TECHNOLOGIES**

1593 ChatGPT was employed to improve writing style and grammar checks. The authors carefully reviewed,
1594 edited, and revised the content according to their own preferences, assuming ultimate responsibility for the
1595 publication's content.
1596

1597 **FIGURE LEGENDS**

1598 **Figure 1. BioID of Stress Granules during steady state and stress.** (**a**) Schematics show experimental
1599 workflow of stress granule proximity labelling no stress (top) or stressed state with oxidative stress (bottom)
1600 in human cells. (**b**) Quantitative comparison of average spectra (log_2 transformed) of high-confidence
1601 interactors identified by G3BP1 (top) and FMR1 (bottom) during no stress *vs*. stress state (0.5mM sodium
1602 arsenite (III)) using ProHits-Viz[131]. (**c**) Comparative analyses of carrier pre-treated stress BioID (top) *vs.*
1603 lipoamide pre-treated stress BioID (bottom). The condition-condition plot shows the abundance of high-
1604 confidence interactors identified by G3BP1 in each condition. (**d**) Schematics of nine high-information baits
1605 and their subcellular location. Baits with asterisks localize to multiple compartments. (**e**) Diagram of stress
1606 BioID experimental workflow. Proximity labelling is performed during no stress, stress (arsenite, As (III);
1607 oxidative stress, or NaCl; hyperosmotic stress), or recovery periods for 30 min. (**f**) Western blot shows
1608 eIF2α phosphorylation status in cells used for BioID (HEK293 Flp-In T-REx cells) during no stress (NS),
1609 oxidative (As(III)) or hyperosmotic stress (NaCl) used for BioID.
1610
1611 **Figure 2. Dynamic proteomic landscapes of stress granules** (**a**) Diagram depicting stepwise DIA data
1612 analysis pipeline to improve identification and quantification. (**b**) Bar graph shows comparison to other
1613 existing datasets. Colours indicate overlap with literature-curated stress granule proteins (red), shared with
1614 another dataset but not annotated as stress granule proteins (orange), and unique to each dataset (blue).
1615 Youn *et al.,* 2018 dataset includes high-confidence proximal interactors identified by 58 stress granule
1616 proteins under no stress condition. (**c**) Venn diagram summarizes the overlap between high-confidence
1617 interactors identified in no stress (T1), T2 in oxidative stress (T2_As(III)), and hyperosmotic stress
1618 (T2_NaCl) by one or more baits. (**d**) Heatmap display of hierarchical clustering analysis of statistically
1619 significant proximal interactors identified by at least two baits in stress BioID DIA data (BFDR≤0.03). Baits
1620 and conditions are clustered on the x-axis, and high-confident interactors are clustered on the y-axis based
1621 on their abundance. Boxed areas in red highlight proximal interactions that drive clustering of baits in
1622 T2_NaCl condition compared to other conditions in green. (**e**) Dot Plot visualizes the Gene Ontology terms
1623 enriched in each cluster indicated in panel (d). (**f**) Venn diagram of high-confidence interactors displaying
1624 ≥1.5-fold change in two baits or more from no stress (T1) to stress condition (T2).
1625

1626 **Figure 3. A genome-wide lipoamide suppressor screen identifies components of the CCR4-NOT**
1627 **complex to bypass the lipoamide effect on stress granules.** (**a**) Schematics showing genome-wide
1628 CRISPR Cas knock-out screen to identify genes required for lipoamide inhibitory activity on stress granule

1629 formation. (**b**) A rank-ordered visualization of candidate genes whose knock-out results in suppression of
1630 lipoamide activity, including its known target, SRSF1. (**c**) Secondary siRNA screen and their results.
1631 Lipoamide suppressors validated in oxidative stress condition are indicated in a box (filled in red). Targeting
1632 a subset of genes resulted in constitutive induction of stress granules in the absence of stress (filled in gray;
1633 no box). (**d**) Representative images of validated lipoamide suppressors. Magenta dot: high-confidence
1634 interactors in this stress BioID dataset. Scale bar = 20 μM. (**e**) Examination of individual CCR4-NOT
1635 complex components on their requirements for lipoamide activity on stress granules using siRNA-mediated
1636 knockdown in HeLa cells (top). Cells were pretreated with 5 μM of lipoamide, then stressed with 1 mM of
1637 potassium arsenate (As(V)) (additional lipoamide concentration data available in Supporting Data).
1638 Quantification of the percentage of cells with three or more cytosolic FUS-GFP puncta is plotted against
1639 varying lipoamide pre-treatment conditions from three biological replicates of siRNA experiments (bottom).
1640 (**f**) The effect of combined loss of enzymatic subunits via knockout or knockdown on lipoamide activity on
1641 stress granules in HeLa FUS-GFP cells (top). Cells were pretreated with 200 μM of lipoamide, then stressed
1642 with 20 mM of sodium arsenate (As(V)). The percentage of cells with three or more cytosolic FUS-GFP
1643 puncta is plotted using quantifications from two biological replicates of experiments (bottom; * p-value<0.05
1644 t-test).
1645
1646 **Figure 4. Altering Poly(A) lengths affects efficient stress granule assembly.** (**a**) Representative
1647 images show the effect of cordycepin (50 μM, 2 h) on stress granules (G3BP1) and P-bodies (EDC3) during
1648 oxidative stress (sodium arsenite, As(III); 60 μM, 1 h) in HeLaFlp-In T-REx cells. Scale bar = 50 μM. (**b**)
1649 Violin-Box plot of stress granule and P-body numbers in HeLa Flp-In T-REx cells pretreated with increasing
1650 concentrations of cordycepin for 2 h, followed by no treatment or combined with sodium arsenite, As(III)
1651 stress (60 μM or 75 μM, 1 h). Quantifications from three biological replicates were assessed with Mann
1652 Whitney test for statistical significance compared to 0 cordycepin treatment (*** $p_{adj} < 10^{-3}$, **** $p_{adj} < 10^{-4}$).
1653 (**c**) Violin-Box plot shows the effect of loss of specific CCR4-NOT components on stress granule numbers
1654 (cytoplasmic FUS-GFP) during oxidative stress (1mM sodium arsenate, As(V), 1 h). The number of stress
1655 granules in siRNA-treated samples *vs.* control tested from three biological replicates of siRNA experiments
1656 is assessed for statistical significance using the Mann-Whitney test (**** $p_{adj} < 10^{-4}$). Red dotted line: the
1657 median stress granule number in control. (**d**) Bar graph visualization of the effect of CNOT1 knockdown on
1658 stress granule formation during oxidative stress (1mM potassium arsenate, As(V)) in HeLa cells pretreated
1659 with conditions that inhibit stress granule formation (cordycepin, 10 μM lipoamide, or cordycepin and 10 μM
1660 lipoamide combined). The sequence of treatments is shown in the top panel. The bar graph depicts data
1661 from three biological replicates, quantified from over 300 cells. (**e**) Model of two paralleled mechanisms
1662 driving stress granule formation. Lengthening global poly(A) tails promotes stress granule formation by
1663 providing longer RNAs for PABPC1 scaffolding. The CCR4-NOT complex and cordycepin shorten Poly(A)
1664 tails, preventing efficient stress granule formation. Lipoamide blocks the oxidation of RNA-binding proteins
1665 that promote stress granule formation[56].

1666

1667 **Figure 5. Stress Granule localization of the CCR4-NOT complex.** (**a**) Immunofluorescence microscopy
1668 of CNOT1 (green), P-body marker EDC3 (red), and nuclei (DAPI) in HeLa cells at steady state and stress
1669 conditions (500 μM sodium arsenite, As(III), 30 min or 0.2 M NaCl, 1 h). Scale bar = 10 μM. (**b**)
1670 Immunofluorescence microscopy of CNOT1, CNOT2, CNOT7 and CNOT8 (green), stress granule marker
1671 G3BP1 (red), and nuclei (DAPI) during oxidative (sodium arsenite, As(III), 500 μM, 30 min) and
1672 hyperosmotic stress (sodium chloride, 0.2 M, 1 h) in HeLa cells. Line plots represent the fluorescent
1673 intensity included in the selected insets. Scale bars = 10 μM and 3 μM (from left to right zoomed insets).
1674 (**c**) Dot plot visualization of CNOT2 proximal interactions with the rest of the CCR4-NOT complex subunits
1675 during no stress (T1) and oxidative stress (T2_As(III)). (**d**) Lightning mode confocal microscopy of CNOT1
1676 (green), stress granule marker G3BP1 (red), and nuclei (DAPI) during oxidative stress (sodium arsenite,
1677 As(III), 75 μM, 1 h) and at steady state in HeLa cells. Scale bars = 10, 2 and 1 μM (from left to right zoomed
1678 insets).
1679

1680 **Figure 6. Nanopore direct RNA sequencing demonstrates that sequestration of CCR4–NOT into**
1681 **stress granules promotes poly(A) tail lengthening of stress-survival transcripts.** (**a**) Schematic
1682 showing experimental design for the transcriptomics analysis performed using Nanopore direct RNA
1683 sequencing (DRS). Abundance and poly(A) length measurements were extracted from the direct RNA
1684 sequencing data. (**b**) Transcriptome-wide distribution of gene-level average poly(A) lengths during no
1685 stress, stress and lipoamide+stress, with the average values indicated in the middle of each violin plot.
1686 Groups indicated the entire transcriptome (left), or subgroups of transcripts categorized based on their
1687 enrichment in stress granules (right). Mann-Whitney U test on three biological replicates was performed
1688 with Bonferroni correction to determine significant differences in poly(A) length distributions (** padj <10-2,
1689 **** padj <10-4). (**c**) Volcano plot of poly(A) length fold-changes from no stress to stress (As(V)), and stress
1690 (As(V)) to lipoamide + stress (As(V)) and associated adjusted p-values as determined by TAILCaller and
1691 subsequent post-hoc tests. A >|1.3|-fold cut-off for fold-change was used (n=3). (**d**) Sankey plot shows the
1692 distribution of transcripts whose poly(A) tail lengths were significantly changed in both condition-condition
1693 comparisons and their direction of change. (**e**) Volcano plot of abundance fold-changes from no stress to
1694 stress (As(V)), and stress (As(V)) to lipoamide + stress (As(V)), and associated adjusted p-values, as
1695 determined by DESeq2. A >|1.5|-fold cut-off for fold-change was used (n=3). (**f**) Sankey plot shows the
1696 distribution of transcripts whose abundances were significantly changed in both condition-condition
1697 comparisons and their direction of change. (**g**) A Venn diagram shows genes whose significant changes in
1698 either poly(A) lengths or abundance upon stress were reversed in lipoamide+stress conditions. The 15
1699 shared genes all show stress-induced increases in poly(A) tail length and transcript abundance, changes
1700 that are fully reversed by lipoamide treatment. (**h**) Schematics show a proposed model for stress granule
1701 function in post-transcriptional regulation. Upon stress, the CCR4-NOT complex is sequestered to stress
1702 granules, resulting in poly(A) tail lengthening of stress-survival transcripts, promoting stress adaptation.
1703

1704 **SUPPLEMENTAL INFORMATION**

1705 **Figure S1. Stress BioID quality control** (**a**) Western blot analysis comparing the levels of stably expressed
1706 miniTurbo-tagged proteins to the corresponding endogenous proteins. Lysates prepared from HEK293 Flp-
1707 In T-REx parental cell line, tetracycline-induced miniTurbo stable cells or uninduced cells were analyzed for
1708 each stress granule bait protein (top). Ponceau staining of the total blot is used as a loading control (bottom).
1709 Left: G3BP1 and Right: FMR1. (**b**) Immunofluorescence microscopy of miniTurbo-3xFLAG-G3BP1 cells
1710 under no stress or stressed with sodium arsenite, As(III), then BioID labeled. Stress granule marker (TIA1),
1711 bait (FLAG) and biotinylated proteins (Strep). Scale bar = 10 μM. (**c**) Lipoamide titration test to determine
1712 effective concentration for stress granule inhibition in BioID cells. Quantifications from 2,600-4,300 cells.
1713 (**d**) Condition-condition plot of miniT-G3BP1 high-confidence proximal interactors in cells incubated with a
1714 carrier (DMSO) or 100 μM lipoamide for 1 h, then biotin labelling in 'no stress' state. (**e**) Venn diagram
1715 comparison of high-confidence preys identified from 58 high-specificity baits from Youn *et al.,* 2018 (red),
1716 high-confidence preys of the selected nine baits (green) and literature-curated stress granule proteome
1717 (Tier 1; Youn *et al.,* 2019).
1718

1719 **Figure S2. Stress granule assembly and disassembly kinetics.** (**a**) Immunofluorescence microscopy
1720 images of HEK293 Flp-In T-REx cells fixed and stained for stress granules (G3BP1) at 1 h (left) or 1.5 h
1721 after recovery post oxidative stress. Scale bar = 10 μM. (**b**) Immunofluorescence microscopy images show
1722 stress granule assembly kinetics after hyperosmotic stress (0.2 M NaCl) for indicated times in HEK293 Flp-
1723 In T-REx cells. Stress granule marker G3BP1 (green); P-body marker EDC3 (red); Nuclei (DAPI). Scale
1724 bar = 10 μM. (**c**) Subcellular localization of BioID bait (FLAG), biotinylated proximal proteins (Strep), and
1725 stress granules (TIA1) after 30 min of biotin labeling in hyperosmotic stress condition in miniT-3xFLAG-
1726 G3BP1 HEK293 cells. Scale bar = 10 μM. (**d**) Stress granule dissolution kinetics after hyperosmotic stress
1727 in HEK293 Flp-In T-REx cells at 1 min (left) or 30 min after recovery. Scale bar = 10 μM. (**e**) Schematics of
1728 biotin labeling performed in stress BioID timecourse experiments. (**f**) Western blot analysis of puromycin
1729 incorporation for 10 min during the indicated stress and recovery periods. NS = No stress, As(III) (sodium
1730 arsenite, 500μM, 35 min), NaCl (0.2M, 35 min). (**g**) Overview of stress BioID experiments performed.
1731

1732 **Figure S3. Hyperosmotic stress induces proximal associations with microtubule-associated**
1733 **proteins.**
1734 (**a**) Dot plot visualization of selected high-confidence preys identified in DDX3X stress BioID timecourse.
1735 As(III) (sodium arsenite, 500μM, 5'-35'), NaCl (0.2M, 45'-75'). (**b**) Schematics show alternative
1736 hyperosmotic stress timecourse set up (top). Dot plot visualization of selected high-confidence preys
1737 identified by DDX3X during alternative hyperosmotic stress conditions (bottom). (**c**) Heatmap visualization
1738 of hierarchical clustering of high-confidence preys identified in DCP1A and DDX3X stress BioID. Baits and
1739 conditions are clustered on the x-axis, and high-confidence interactors are clustered on the y-axis based
1740 on their abundance.

1741

1742 **Figure S4. DIA analysis improves data quality.** (**a**) Illustration of Data-Dependent Acquisition (DDA) *vs.*
1743 Data-Independent Acquisition (DIA) methods in mass spectrometry. (**b**) Diagram of BioID DIA analysis
1744 workflow. (**c**) Bar graph of identified proteins in each BioID time-course experiment using DDA and DIA
1745 methods. Error bars show variation between replicates. (**d**) Violin plots show the pairwise Jaccard indices
1746 between BioID samples. Each point represents a pairwise sample comparison. Statistical significance for
1747 three groups of pairwise comparison was evaluated using Mann Whitney U-tests.

1748

1749 **Figure S5. Pearson correlation analysis of processed DIA data.** Heatmap displays the Pearson
1750 correlation coefficient calculated between all DIA samples acquired prior to statistical analysis using
1751 SAINTq.

1752

1753 **Figure S6. Total proteome changes upon stress, stress-induced proximal interaction changes and**
1754 **validation of interactors.** (**a**) Volcano plot shows total proteome abundance changes in oxidative stress
1755 (As (III), sodium arsenite, 0.5mM) or hyperosmotic stress (0.2M NaCl) conditions. Vertical lines indicate
1756 1.5-fold changes. (**b**) The violin plot shows the distributions of abundance fold-changes in high-confidence
1757 interactors during stress time course. (**c**) Colocalization validation of identified high-confidence interactors
1758 to stress granules in HeLa Flp-In T-REx cells. TRIM56 (endogenous); LARP6-mCherry (stable expression).
1759 Scale bar = 10 μM.

1760

1761 **Figure S7. Localization of large ribosomal subunits during oxidative and hyperosmotic stress**. (**a**)
1762 Left: Representative images of HeLa cells treated with As(III) (0.5mM sodium arsenite) or 0.2M NaCl for 30
1763 min were permeabilized with 0.01% digitonin, then fixed and processed for immunofluorescence
1764 microscopy of RPL32 and G3BP1. Middle: Colocalization is assessed using a line graph on selected stress
1765 granules. Right: Images of selected stress granules. Scale bar = 2 μM. (**b**) Left: Representative images of
1766 immunofluorescence microscopy of RPL36 and G3BP1, same conditions as panel a. Middle: Colocalization
1767 is assessed using a line graph on selected stress granules. Right: Images of selected stress granules.
1768 Scale bar = 2 μM. (**c**) Pearson correlation coefficient (PCC) analysis between the RPL32 and G3BP1
1769 channels. A t-test was used to determine the statistical significance of changes in the extent of colocalization
1770 between untreated (UT), As(III) and NaCl groups with Holm adjustment (ns, non-significant, n= 2 biological
1771 replicates). (**d**) Pearson correlation coefficient (PCC) analysis between the RPL36 and G3BP1 channels. A
1772 t-test was used to determine the statistical significance of changes in the extent of colocalization between
1773 untreated (UT), As(III) and NaCl groups with Holm adjustment (ns, non-significant, * padj <0.05, n= 2
1774 biological replicates).

1775

1776 **Figure S8. Dynamic Interactions of the CCR4-NOT complex, Protein quantification of CCR4-NOT**
1777 **complex upon knockout or knockdown and the effect of cordycepin on PABPC1.** (**a**) Volcano plot

1778 shows abundance changes in G3BP1 high-confidence interactors during steady to stress state transition.
1779 (**b**) CCR4-NOT complex abundance in Cas12a-mediated knockout and/or esiRNA-mediated knockdown
1780 HeLa cells used for stress granule quantifications in Figure 3F. Protein abundance information was obtained
1781 using DIA mass spectrometry analysis of processed cell lysates collected in no stress condition. Protein
1782 abundance is normalized to their abundance in control (no gRNA and scrambled esiRNA) (**c**)
1783 Representative images show the effect of cordycepin (50 μM, 2 h) on G3BP1 and PABPC1 during oxidative
1784 stress (sodium arsenite (III); 60 μM, 1h) in HeLaFlp-In T-REx cells. Scale bar = 50 μM. (**d**) Violin-Box plot
1785 of PABPC1 puncta numbers in HeLa Flp-In T-REx cells pretreated with increasing concentrations of
1786 cordycepin for 2 h, followed by no treatment or combined with sodium arsenite (III) stress (60 μM or 75 μM,
1787 1 h). Quantifications from three biological replicates were assessed with Mann Whitney test for statistical
1788 significance compared to 0 cordycepin treatment (**** $p_{adj} < 10^{-4}$).
1789
1790 **Figure S9. Subcellular localization of CCR4-NOT complex.** (**a**) Top two rows: Immunofluorescence
1791 microscopy of HEK293 Flp-In T-REx cells in no stress or stressed conditions (500 μM sodium arsenite,
1792 As(III), 30 min or 0.2 M sodium chloride, 1 h). Bottom panel shows images of HEK293 Flp-In T-REx cells
1793 inducibly and stably expressing DCP1A-3xFLAG construct. CNOT1 (green), P-body marker EDC3 (red),
1794 nuclei (DAPI). Scale bar = 10 μM. (**b**) Immunofluorescence microscopy of HEK293 Flp-In T-REx cells in
1795 no stress or stressed conditions (500 μM sodium arsenite, As(III), 30 min or 0.2 M sodium chloride, 1 h).
1796 CNOT1, CNOT7, or CNOT8 (red) paired with stress granule marker G3BP1 (green), nuclei (DAPI). Intensity
1797 line plot made in Fiji. Scale bar = 10 μM. (**c**) Immunofluorescence microscopy of CNOT2-3xFLAG stable
1798 cells, untreated or stressed for 30 min, stained for stress granule marker (G3BP1) and FLAG tag on CNOT2-
1799 3xFLAG construct. Scale bar = 10 μM. (**d**) Live cell images of HeLa stable cells inducibly expressing mNeon
1800 tagged CCR4-NOT component and mScarlet-G3BP1, stressed with 500 μM sodium arsenite, As(III) for 30
1801 min. Scale bar = 10 μM.
1802
1803 **Figure S10. CNOT1 sensitivity to cycloheximide.** (**a**) Top: Experimental workflow showing how cells
1804 were stressed with 60μM sodium arsenite (As(III)) for 1 h, then treated with carrier or cyclohexamide (CHX,
1805 10μg/mL) for 0.5 h or 1 h. Bottom: Representative immunofluorescence microscopy images show
1806 dissolution of stress granules (G3BP1) and CNOT1 upon CHX treatment. Scale bar = 50 μM.
1807
1808 **Figure S11: Global transcriptomic analysis of stress-induced poly(A) lengths and abundance**
1809 **changes dependent on stress granules**. (a) Immunofluorescence microscopy images of HeLa cells in no
1810 stress, stressed (sodium arsenate, As(V) 20mM, 1 h) or stress with lipoamide pretreatment (200μM, 1 h
1811 pretreatment, then continued for 1 h during stress) conditions stained for endogenous CNOT1 and stress
1812 granule marker G3BP1 (green). Scale bar = 50 μM, and 20 μM for enlarged view. (b) Transcriptome-wide
1813 distribution of gene-level average poly(A) lengths during no stress (n=3), stress (n=3), lipoamide+stress
1814 (n=3), and lipoamide (n=1) with the average values indicated in the middle of each violin plot. Poly(A)

1815 lengths were compared for the whole dataset. Mann-Whitney-U test on average of three biological
1816 replicates for no stress, arsenate As(V), lipoamide + arsenate As(V), and one replicate for lipoamide alone,
1817 Bonferroni correction (**** padj $<10^{-4}$). (c) Density plots showing poly(A) length distributions for JUN and
1818 FOS transcripts during no stress, stress (As(V)), and lipoamide + stress (As(V)). TAILcaller is used to
1819 determine transcripts with significant changes in poly(A) tail distribution. For the JUN and FOS transcript
1820 examples, the Kruskal-Wallis test was employed to determine statistical significance. (d) (Left) Volcano plot
1821 of poly(A) length fold-changes from no stress to lipoamide + stress (As(V)) and associated adjusted p-
1822 values as determined by TAILCaller and subsequent post-hoc tests. A 1.3-fold cut-off for fold-change was
1823 used (n=3). (Right) Volcano plot of abundance fold-changes from no stress to lipoamide + stress (As(V)),
1824 and associated adjusted p-values, as determined by DESeq2. A 1.5-fold cut-off for fold-change was used
1825 (n=3).
1826
1827 **Figure S12**: **Analysis of transcripts regulated by CCR4-NOT sequestration to stress granules, and**
1828 **validation of DESeq2**. (a) Dotplot visualization of GO analysis of genes with significant changes during
1829 stress, reversed by lipoamide, in both their poly(A) length and abundance (shared changes), poly(A)
1830 changes only, or abundance only. Selected GO terms were ordered based on the fraction of genes that
1831 belonged to the indicated GO term amongst the total significant list. (b) Bar plot of median poly(A) lengths
1832 for 15 genes with significant poly(A) length and abundance changes, which were reversed by lipoamide
1833 (n=3, median value taken from all 3 replicates). All genes were significant and made the 1.3-fold-change
1834 cut-off in no stress *vs.* stress and stress *vs.* lipoamide+stress, except GAPDH and GADD45A, which show
1835 non-significant changes. (c) Bar plot of $\log_{10}$(RPM) for 14 genes with significant poly(A) length and
1836 abundance changes, which were reversed by lipoamide; two control genes, GAPDH and GADD45A, used
1837 for RT-qPCR validation were also included (n=3). All genes were significant and made the 1.5-fold-change
1838 cut-off, except GAPDH and GADD45A, which are included as a comparison. (d) RT-qPCR quantification of
1839 transcript abundance, testing candidate genes which were significantly increased during stress (As(V)) and
1840 reversed by lipoamide (n=3). Abundance is normalized to the 'unstressed' condition. Pairwise t-test was
1841 performed on three biological replicates, Bonferroni correction (* padj <0.05, ** padj $<10^{-2}$). (e) RT-qPCR
1842 quantification of transcript abundance, testing candidate genes which were significantly decreased during
1843 stress (As(V)) (n=3). Abundance is normalized to 'unstressed' condition Pairwise t-test was performed on
1844 three biological replicates, Bonferroni correction (* padj <0.05, ** padj $<10^{-2}$).
1845
1846 **Table S1.** Stress BioID of G3BP1 and FMR1 during oxidative stress and Stress BioID of G3BP1 with
1847 lipoamide pre-treatment, related to Figure 1B-C.
1848 **Table S2.** High Information Bait Selection, related to Figure 1D.
1849 **Table S3.** Stress BioID of Nine Stress Granule or Stress Granule& P-body baits during stress and
1850 alternative hyperosmotic stress conditions analyzed in DDA mode.

1851 **Table S4.** Stress BioID of Nine Stress Granule or Stress Granule& P-body baits during stress analyzed in
1852 DIA mode, related to Figure 2.
1853 **Table S5.** Analysis of Conserved High-Confidence Proximal Interactors, related to Figures 2D-E.
1854 **Table S6.** Linear Mixed Model ANOVA Analysis to Determine Differentially Interacting Proximal Interactors,
1855 related to Figure 2F.
1856 **Table S7.** Total Proteome Abundance Changes during Oxidative Stress (0.5mM sodium arsenite, As(III))
1857 and Hyperosmotic Stress (0.2M NaCl) using mixed model ANOVA Analysis to Determine Differential
1858 Abundant Proteins, related to Figures S6A.
1859 **Table S8.** Nanopore DRS results, measuring transcriptome abundance and poly(A) lengths, related to
1860 Figure 6.
1861 **Table S9**. RT-qPCR primer information, related to Figure S11D-E.
1862

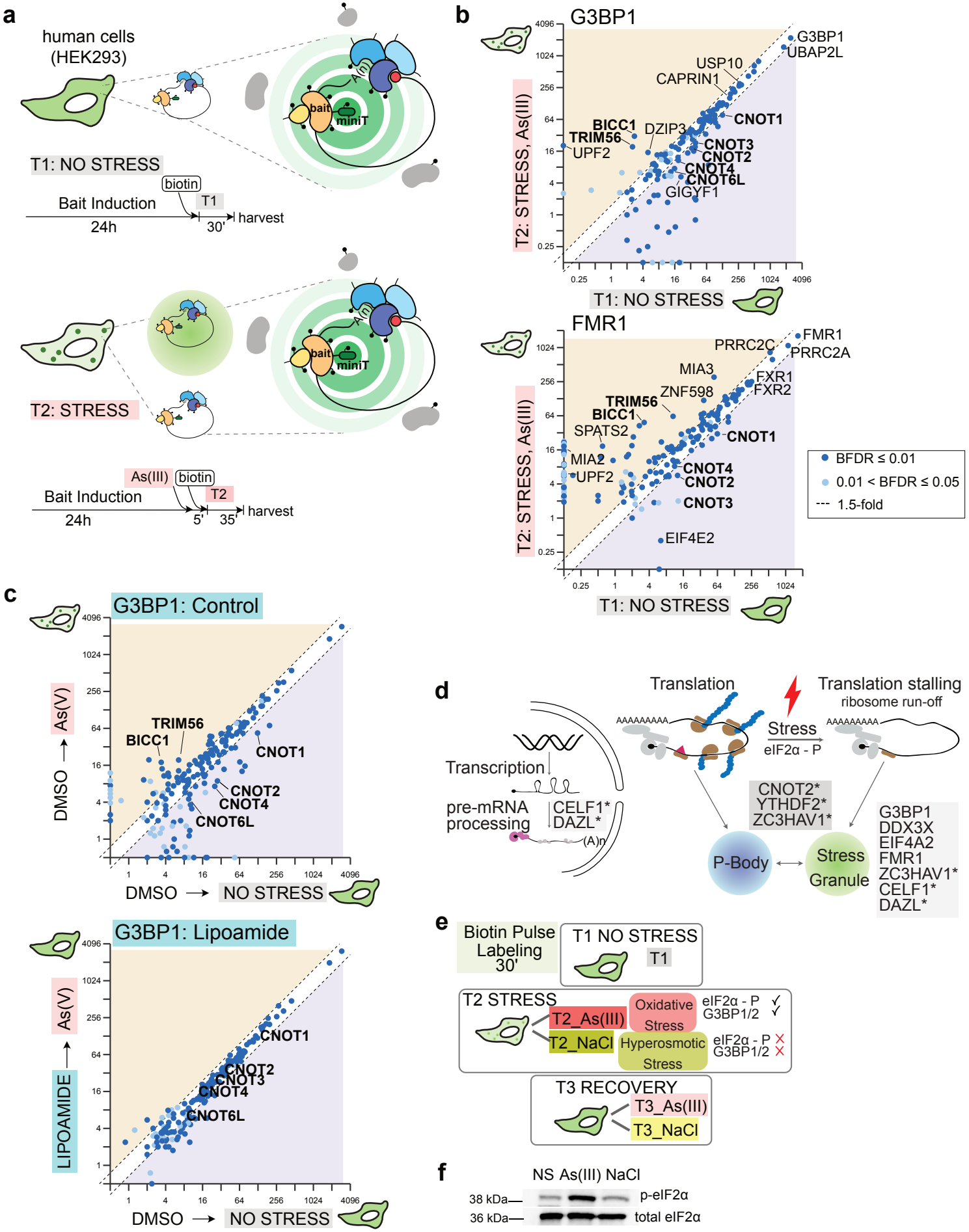
a
human cells
(HEK293)
bait
miniT
A(n)
T1: NO STRESS
biotin
Bait Induction
T1
24h
30'
harvest
T2: STRESS
As(III)
biotin
Bait Induction
T2
24h
5'
35'
harvest
b
G3BP1
G3BP1
UBAP2L
USP10
CAPRIN1
CNOT1
BICC1
TRIM56
UPF2
DZIP3
CNOT3
CNOT2
CNOT4
CNOT6L
GIGYF1
T2: STRESS, As(III)
T1: NO STRESS
FMR1
FMR1
PRRC2C
PRRC2A
MIA3
FXR1
FXR2
ZNF598
TRIM56
BICC1
SPATS2
CNOT1
MIA2
UPF2
CNOT4
CNOT2
CNOT3
EIF4E2
BFDR ≤ 0.01
0.01 < BFDR ≤ 0.05
1.5-fold
c
G3BP1: Control
As(V)
DMSO
TRIM56
BICC1
CNOT1
CNOT2
CNOT4
CNOT6L
DMSO → NO STRESS
G3BP1: Lipoamide
As(V)
LIPOAMIDE
CNOT1
CNOT2
CNOT3
CNOT4
CNOT6L
DMSO → NO STRESS
d
Translation
Translation stalling
ribosome run-off
Stress
eIF2α - P
Transcription
pre-mRNA processing
CELF1*
DAZL*
CNOT2*
YTHDF2*
ZC3HAV1*
P-Body
Stress Granule
G3BP1
DDX3X
EIF4A2
FMR1
ZC3HAV1*
CELF1*
DAZL*
e
Biotin Pulse Labeling 30'
T1 NO STRESS
T1
T2 STRESS
T2_As(III)
T2_NaCl
Oxidative Stress
Hyperosmotic Stress
eIF2α - P
G3BP1/2
T3 RECOVERY
T3_As(III)
T3_NaCl
f
NS As(III) NaCl
38 kDa
36 kDa
p-eIF2α
total eIF2α

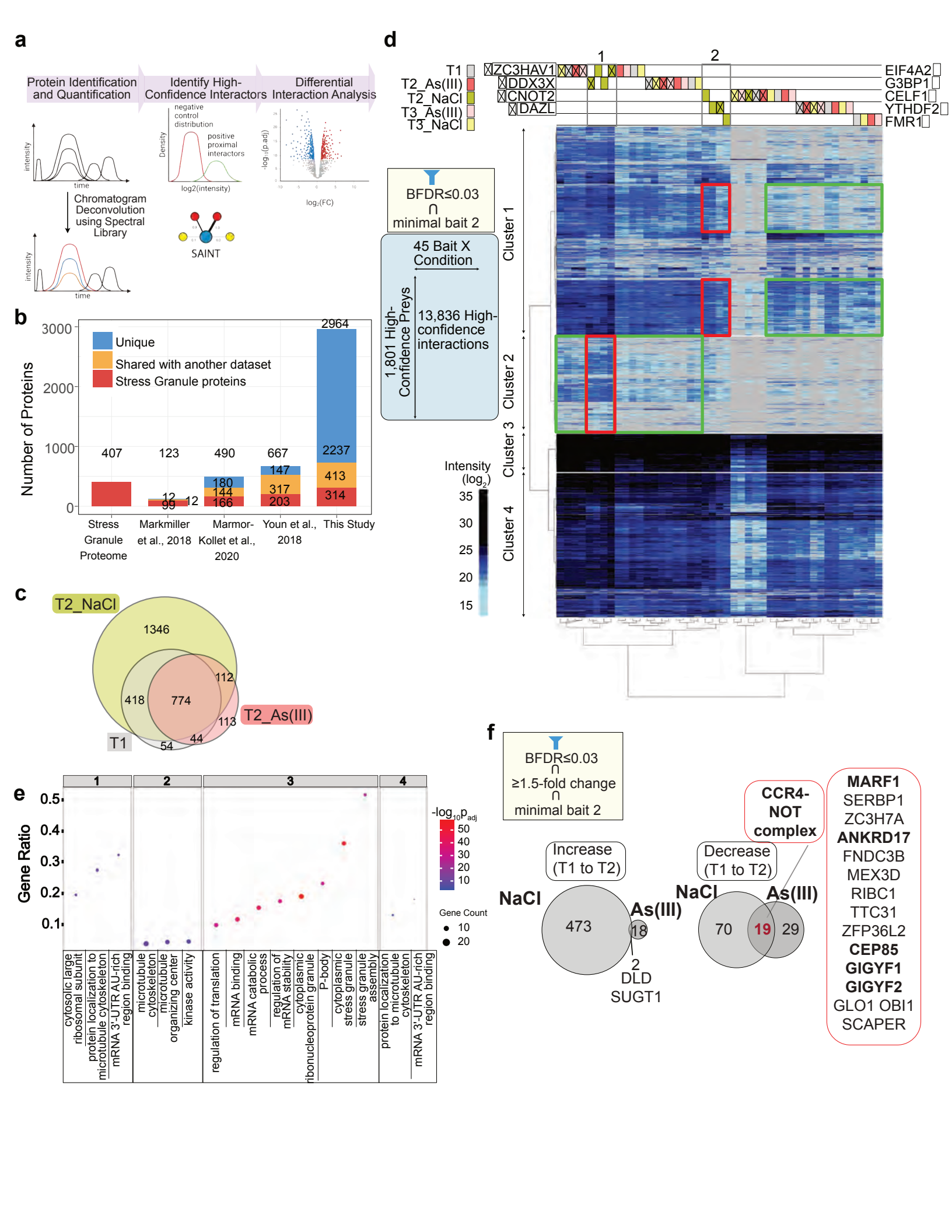
a
Protein Identification and Quantification
Identify High-Confidence Interactors
Differential Interaction Analysis
intensity
time
Chromatogram Deconvolution using Spectral Library
negative control distribution
positive proximal interactors
Density
log2(intensity)
SAINT
log2(FC)
b
Unique
Shared with another dataset
Stress Granule proteins
Number of Proteins
3000
2000
1000
0
407
123
490
667
2964
2237
413
314
147
317
203
180
144
166
12
99
12
Stress Granule Proteome
Markmiller et al., 2018
Marmor-Kollet et al., 2020
Youn et al., 2018
This Study
c
T2_NaCl
T2_As(III)
T1
1346
112
418
774
113
54
44
d
T1
T2_As(III)
T2_NaCl
T3_As(III)
T3_NaCl
ZC3HAV1
DDX3X
CNOT2
DAZL
EIF4A2
G3BP1
CELF1
YTHDF2
FMR1
BFDR≤0.03
∩
minimal bait 2
45 Bait X Condition
1,801 High-Confidence Preys
13,836 High-confidence interactions
Cluster 1
Cluster 2
Cluster 3
Cluster 4
Intensity (log2)
35
30
25
20
15
e
Gene Ratio
0.5
0.4
0.3
0.2
0.1
-log10padj
50
40
30
20
10
Gene Count
10
20
cytosolic large ribosomal subunit
protein localization to microtubule cytoskeleton
mRNA 3'-UTR AU-rich region binding
microtubule cytoskeleton organizing center
kinase activity
regulation of translation
mRNA binding
mRNA catabolic process
regulation of mRNA stability
cytoplasmic ribonucleoprotein granule
P-body
cytoplasmic stress granule
stress granule assembly
protein localization to microtubule cytoskeleton
mRNA 3'-UTR AU-rich region binding
f
BFDR≤0.03
∩
≥1.5-fold change
∩
minimal bait 2
Increase (T1 to T2)
NaCl
As(III)
473
18
2
DLD
SUGT1
Decrease (T1 to T2)
NaCl
As(III)
70
19
29
CCR4-NOT complex
MARF1
SERBP1
ZC3H7A
ANKRD17
FNDC3B
MEX3D
RIBC1
TTC31
ZFP36L2
CEP85
GIGYF1
GIGYF2
GLO1 OBI1
SCAPER

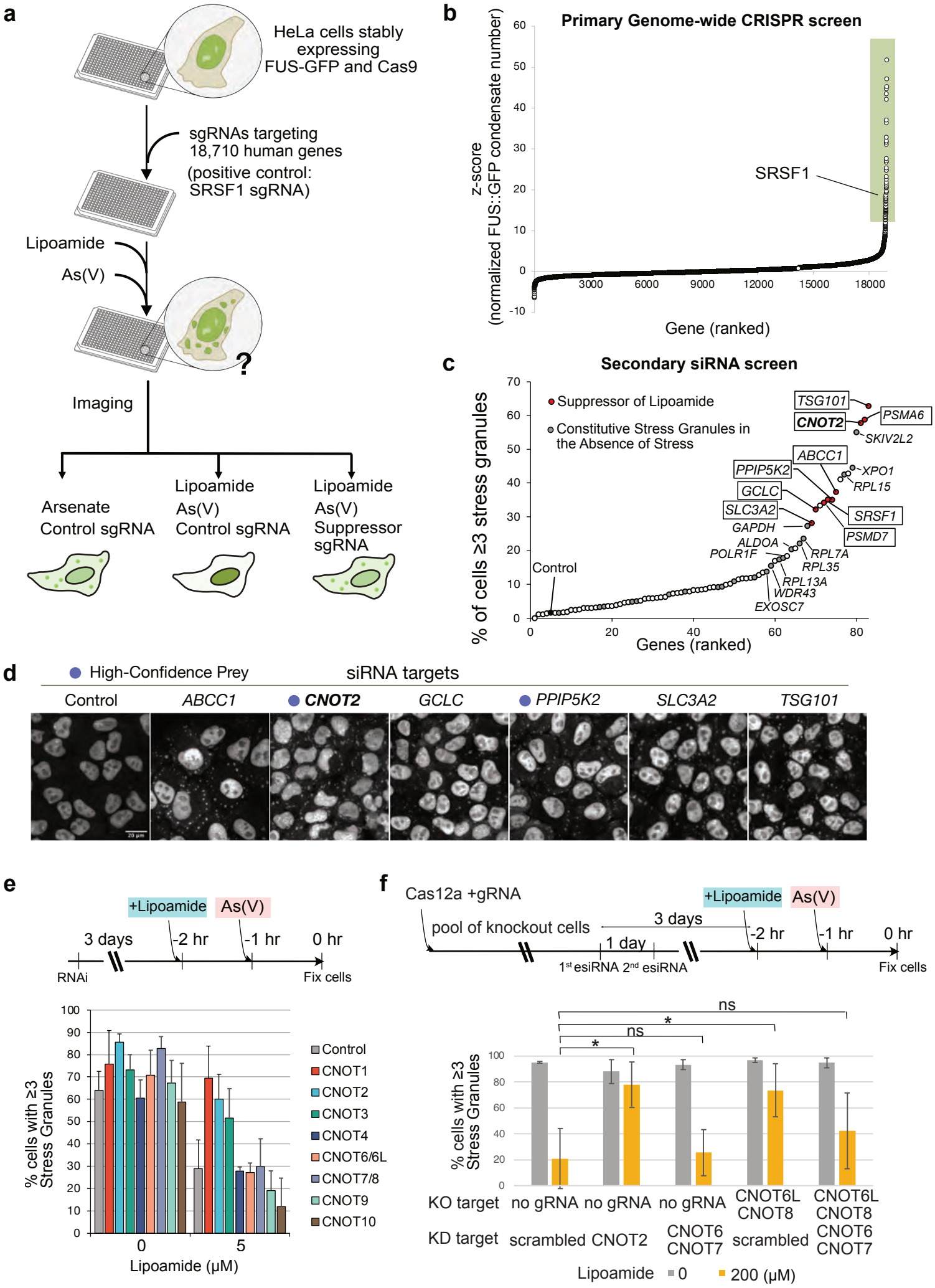
a
HeLa cells stably expressing FUS-GFP and Cas9
sgRNAs targeting 18,710 human genes
(positive control: SRSF1 sgRNA)
Lipoamide
As(V)
?
Imaging
Arsenate
Control sgRNA
Lipoamide
As(V)
Control sgRNA
Lipoamide
As(V)
Suppressor sgRNA
b
Primary Genome-wide CRISPR screen
z-score
(normalized FUS::GFP condensate number)
SRSF1
Gene (ranked)
c
Secondary siRNA screen
Suppressor of Lipoamide
Constitutive Stress Granules in the Absence of Stress
% of cells ≥3 stress granules
Genes (ranked)
Control
TSG101
CNOT2
PSMA6
SKIV2L2
ABCC1
PPIP5K2
XPO1
RPL15
GCLC
SLC3A2
SRSF1
GAPDH
PSMD7
ALDOA
POLR1F
RPL7A
RPL35
RPL13A
WDR43
EXOSC7
d
High-Confidence Prey
siRNA targets
Control
ABCC1
CNOT2
GCLC
PPIP5K2
SLC3A2
TSG101
e
+Lipoamide
As(V)
3 days
-2 hr
-1 hr
0 hr
RNAi
Fix cells
% cells with ≥3 Stress Granules
Lipoamide (μM)
Control
CNOT1
CNOT2
CNOT3
CNOT4
CNOT6/6L
CNOT7/8
CNOT9
CNOT10
f
Cas12a +gRNA
pool of knockout cells
3 days
1 day
1st esiRNA 2nd esiRNA
+Lipoamide
As(V)
-2 hr
-1 hr
0 hr
Fix cells
ns
*
ns
*
% cells with ≥3 Stress Granules
KO target
no gRNA
no gRNA
no gRNA
CNOT6L CNOT8
CNOT6L CNOT8
KD target
scrambled
CNOT2
CNOT6 CNOT7
scrambled
CNOT6 CNOT7
Lipoamide
0
200 (μM)

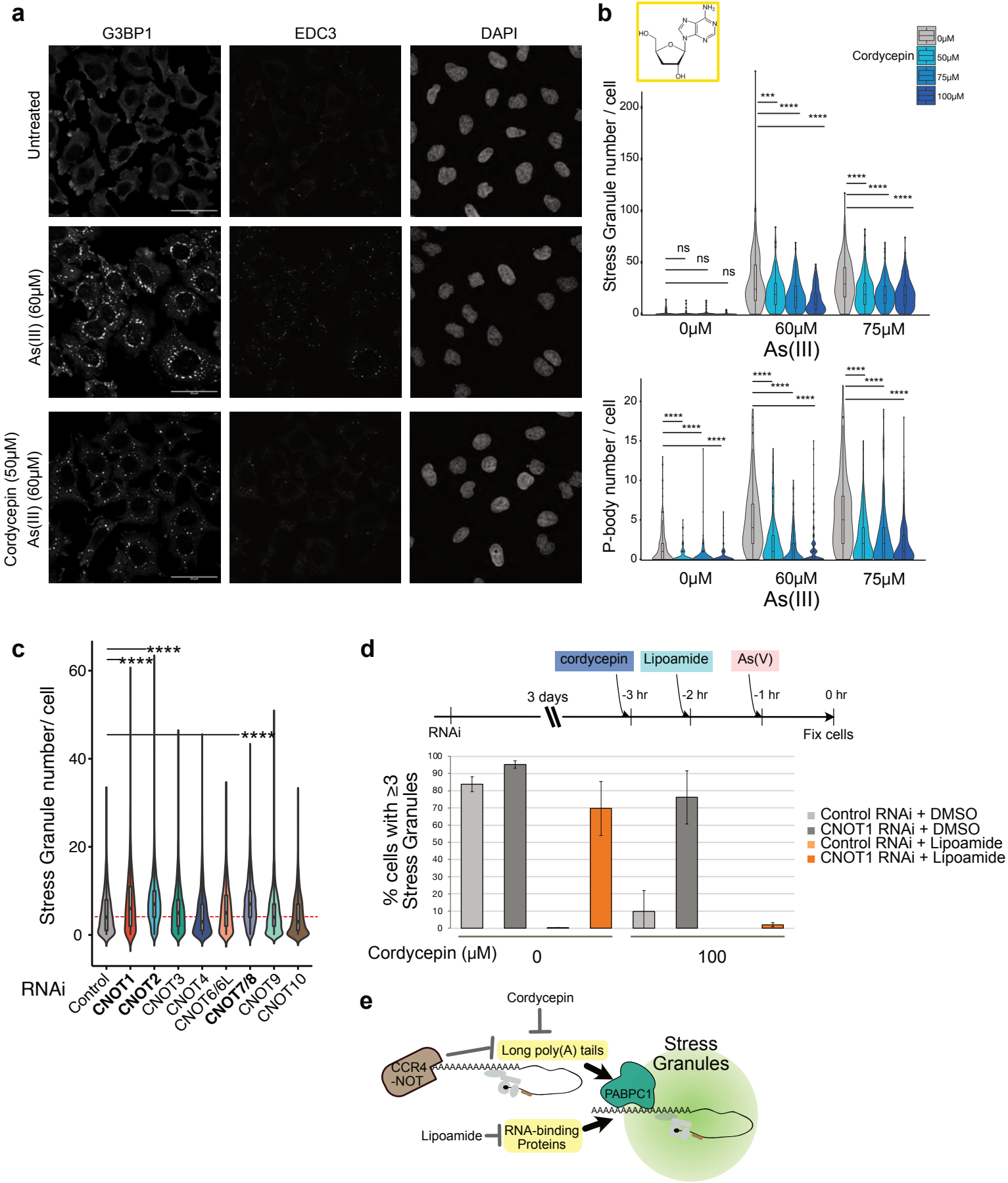
a
G3BP1
EDC3
DAPI
Untreated
As(III) (60μM)
Cordycepin (50μM)
As(III) (60μM)
b
Cordycepin
0μM
50μM
75μM
100μM
Stress Granule number / cell
ns
***
****
0μM
60μM
75μM
As(III)
P-body number / cell
c
Stress Granule number/ cell
RNAi
Control
CNOT1
CNOT2
CNOT3
CNOT4
CNOT6/6L
CNOT7/8
CNOT9
CNOT10
d
cordycepin
Lipoamide
As(V)
3 days
-3 hr
-2 hr
-1 hr
0 hr
RNAi
Fix cells
% cells with ≥3 Stress Granules
Control RNAi + DMSO
CNOT1 RNAi + DMSO
Control RNAi + Lipoamide
CNOT1 RNAi + Lipoamide
Cordycepin (μM)
0
100
e
Cordycepin
Long poly(A) tails
CCR4 -NOT
Stress Granules
PABPC1
Lipoamide
RNA-binding Proteins

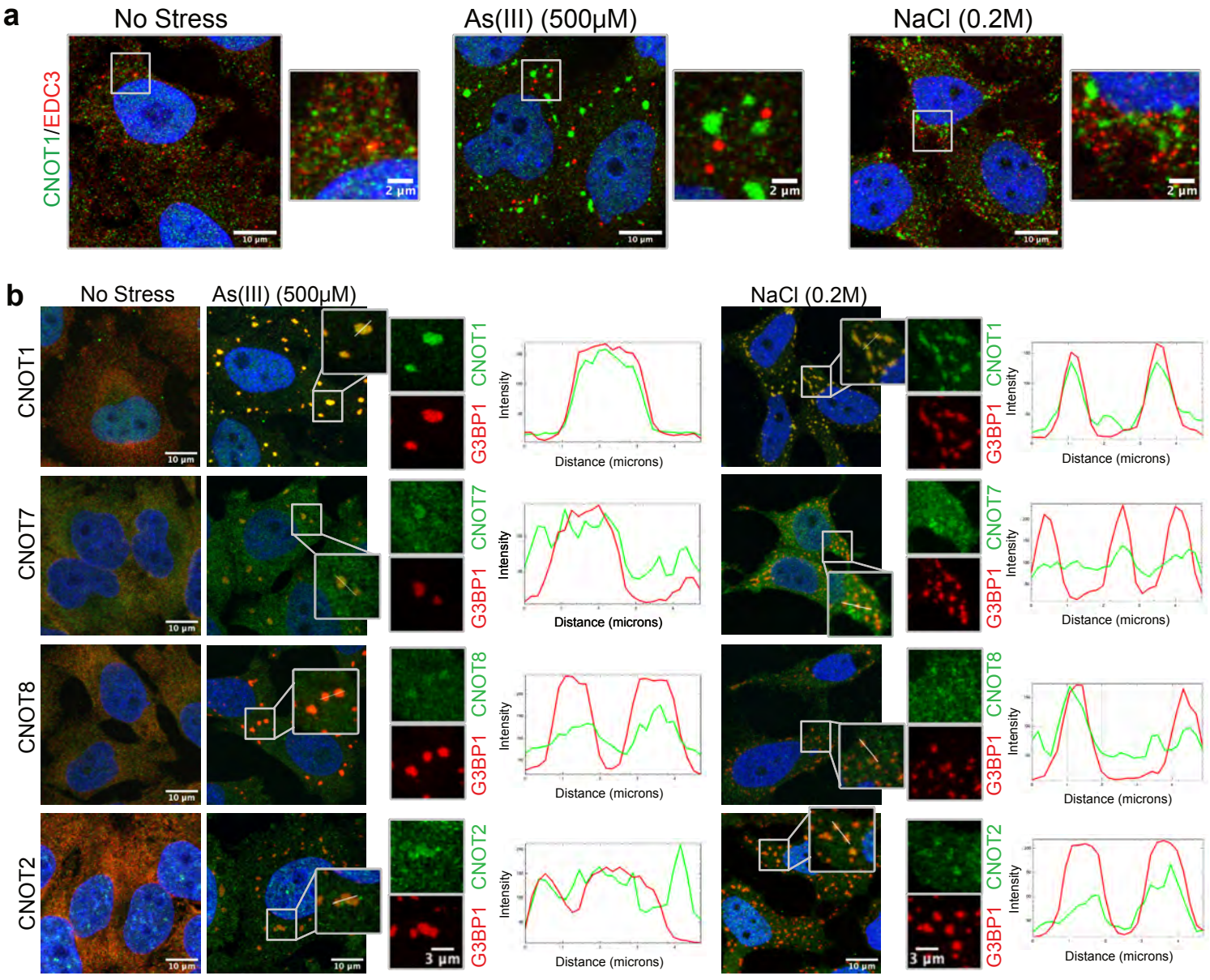
a
No Stress
As(III) (500μM)
NaCl (0.2M)
CNOT1/EDC3
2 μm
10 μm
b
No Stress
As(III) (500μM)
NaCl (0.2M)
CNOT1
CNOT7
CNOT8
CNOT2
G3BP1
Intensity
Distance (microns)
3 μm
c
CNOT2-miniT
As[III]
T1
T2
CNOT1
CNOT2
CNOT3
CNOT4
CNOT6
CNOT6L
CNOT8
CNOT9
CNOT10
Average Prey Intensity
0
50
Relative Prey Intensity
≤ 0.01
≤ 0.03
> 0.03
BFDR
d
Untreated
As(III) (75μM)
G3BP1
CNOT1
1 μm
CNOT1 G3BP1

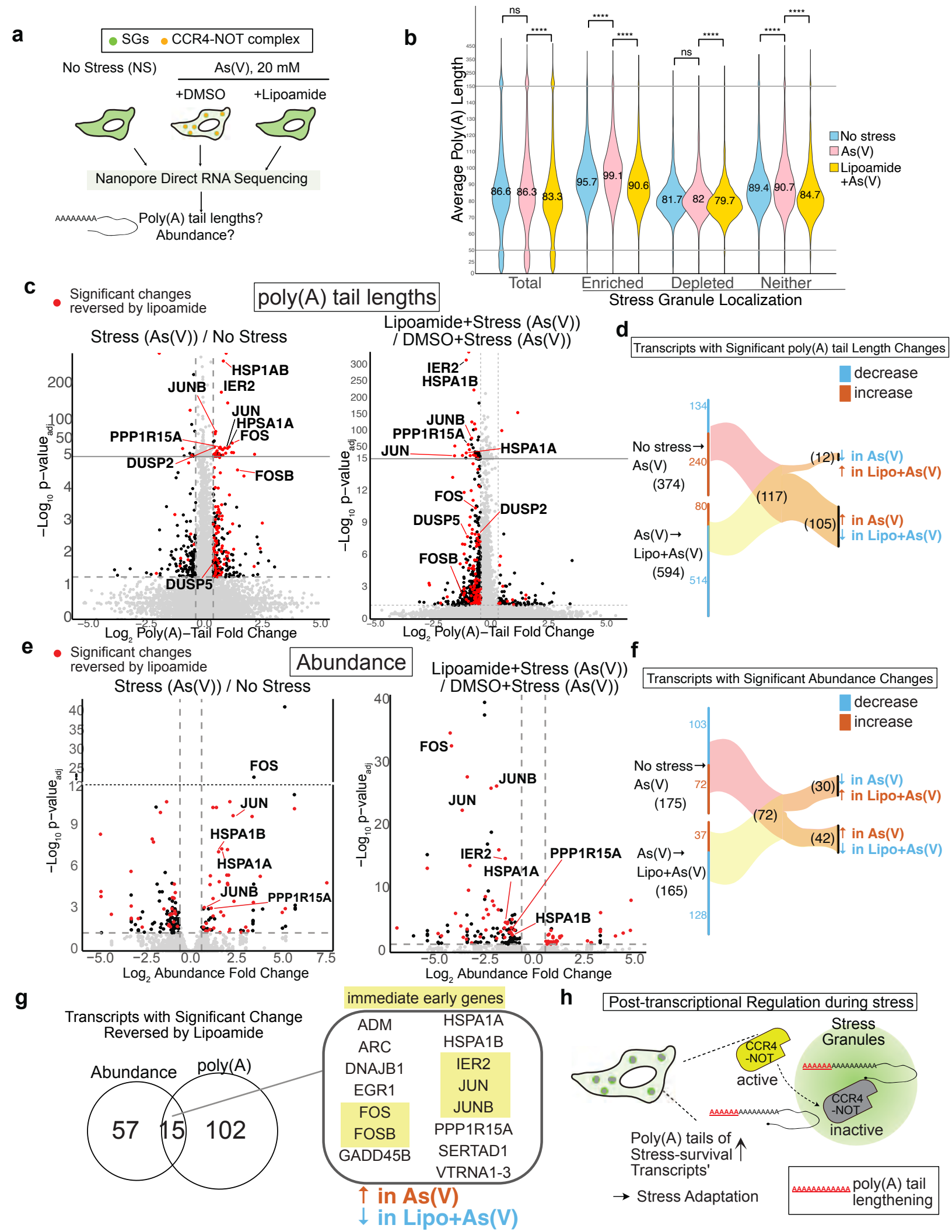
a
SGs
CCR4-NOT complex
No Stress (NS)
As(V), 20 mM
+DMSO
+Lipoamide
Nanopore Direct RNA Sequencing
AAAAAAAA
Poly(A) tail lengths?
Abundance?
b
Average Poly(A) Length
No stress
As(V)
Lipoamide +As(V)
86.6
86.3
83.3
95.7
99.1
90.6
81.7
82
79.7
89.4
90.7
84.7
ns
****
Total
Enriched
Depleted
Neither
Stress Granule Localization
c
Significant changes reversed by lipoamide
poly(A) tail lengths
Stress (As(V)) / No Stress
Lipoamide+Stress (As(V)) / DMSO+Stress (As(V))
HSP1AB
JUNB
IER2
JUN
HPSA1A
FOS
PPP1R15A
DUSP2
FOSB
DUSP5
HSPA1A
−Log10 p−value adj
Log2 Poly(A)−Tail Fold Change
d
Transcripts with Significant poly(A) tail Length Changes
decrease
increase
No stress→ As(V) (374)
As(V)→ Lipo+As(V) (594)
134
240
80
514
(12)
(117)
(105)
↓ in As(V)
↑ in Lipo+As(V)
↑ in As(V)
↓ in Lipo+As(V)
e
Significant changes reversed by lipoamide
Abundance
Stress (As(V)) / No Stress
Lipoamide+Stress (As(V)) / DMSO+Stress (As(V))
FOS
JUN
HSPA1B
HSPA1A
JUNB
PPP1R15A
IER2
−Log10 p−value adj
Log2 Abundance Fold Change
f
Transcripts with Significant Abundance Changes
decrease
increase
No stress→ As(V) (175)
As(V)→ Lipo+As(V) (165)
103
72
37
128
(30)
(72)
(42)
↓ in As(V)
↑ in Lipo+As(V)
↑ in As(V)
↓ in Lipo+As(V)
g
Transcripts with Significant Change Reversed by Lipoamide
Abundance
poly(A)
57
15
102
immediate early genes
ADM
ARC
DNAJB1
EGR1
FOS
FOSB
GADD45B
HSPA1A
HSPA1B
IER2
JUN
JUNB
PPP1R15A
SERTAD1
VTRNA1-3
↑ in As(V)
↓ in Lipo+As(V)
h
Post-transcriptional Regulation during stress
CCR4 -NOT
active
Stress Granules
AAAAAAAAAAAAAAA
CCR4 -NOT
inactive
Poly(A) tails of Stress-survival Transcripts'
→ Stress Adaptation
AAAAAAAAAAA poly(A) tail lengthening